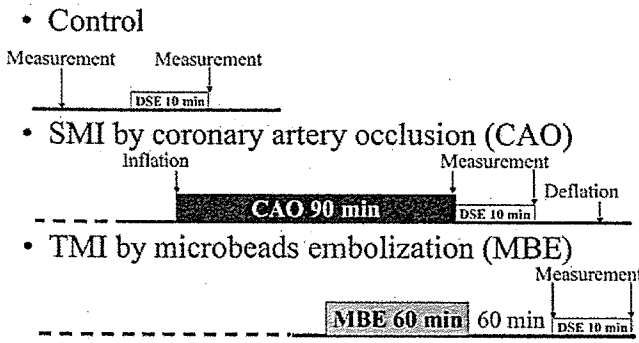

Fig. 1. Experimental protocol. DSE, dobutamine stress echocardiography; SMI, subendocardial myocardial infarction; TMI, transmural myocardial infarction.

(SMI stage; see Refs. 8 and 10), and DSE was performed during balloon inflation. After balloon deflation, 200–300 mg of latex microbeads (diameter 90 μm) were slowly injected in the same artery in 60 min to create a transmural myocardial infarction (TMI stage; see Refs. 7, 12, 15). At the TMI stage, DSE was performed 60 min after microbead embolization to complete myocardial infarction and to avoid ventricular instability to dobutamine challenge, and measurements were done before and after DSE (Fig. 1).

Ultrasound data acquisition. A commercially available ultrasound scanner (PowerVision 8000 3.5-MHz transducer; Toshiba, Tokyo, Japan) was used to obtain the epicardial left ventricular short-axis images at the level of basal and midventricle by tissue Doppler imaging. Recordings were stored in the form of digital loops of two cardiac cycles with 96–102 frames/s for subsequent analysis (33).

Tissue strain imaging. Strain is defined by the equation below and expresses the deformation of an object,

$$\text{Strain} = (L - L_0)/L_0$$

where L_0 is the length of an object before deformation and L is that after or during deformation. In echocardiography, L_0 is usually a muscle length at end diastole, and myocardial strain is used to express the deformation of local myocardial segments (4, 33).

In the present study, myocardial radial strain image was obtained from off-line analysis by using a research software TDI-Q (Toshiba; see Ref. 3). To obtain a strain image, TDI-Q software first calculates the myocardial displacement of all pixels of tissue by integrating myocardial velocity over a certain period. Because the frame rate was 96–102 frames/s, the step size for integration was 9.8–10.4 ms. Next, strain is obtained by evaluating the change of distance between pairs of two points defined on all pixels on the image by utilizing the displacement values. The distance of all two-pixel pairs at the initial time frame is equivalent to "L_0" on the above equation and set at 3 mm in this study (17). The initial time frame is set at end diastole to evaluate contraction; in other words "deformation" of the myocardium occurring in systole.

To measure local strain accurately, it is indispensable to obtain local velocity accurately. Therefore, the present myocardial strain imaging system has adopted tissue Doppler tracking and angle-correction techniques. Tissue Doppler tracking is an automatic motion tracking technique based on tissue Doppler information (30). By integrating a velocity of an indexed point on the ventricular wall known from tissue Doppler imaging, we can obtain myocardial displacement and predict the point where that point moves next. By repeating this procedure, the system can automatically track the motion of the point. With this technique, the influence of myocardial translation can be neglected. The angle-correction technique enables us to partly overcome the Doppler incident angle dependency that is inherent in Doppler echocardiography, as previous reports described (3, 26, 32). To correct the Doppler incident angle, a contraction center is set at the center of the left ventricular cavity at end systole in the left ventricular short-axis view. Next, the software automatically calculates the tissue velocity toward the contraction center (V_{motion}) by dividing the velocity toward a transducer (V_{beam}) by the cosine of the angle (θ) between the Doppler beam and the direction to the contraction center as follows:

$$V_{motion} = V_{beam}/\cos\theta$$

With the use of these two techniques, the research software TDI-Q automatically cancelled the effect of myocardial translation and angle dependency, accurately providing myocardial velocity, displacement, and strain (3). In the previously described experiments, the displacement data obtained by this method correlated with true displacement ($r = 0.99$, $P < 0.0001$; see Ref. 26).

Myocardial radial strain distribution over the myocardium is obtained as M-mode color-coded images, and the profile of distribution (TMSP) at end systole is shown as in Fig. 2. Bright color indicates high strain, and dark color indicates low strain. We obtained TMSP at basal and midinferolateral walls at end systole. We divided the myocardium into subendocardial and subepicardial half-layers by the midpoint of the myocardium at end systole. Mean strain values in the subendocardial half-layer and in the subepicardial half-layer were calculated by averaging strain values over each layer.

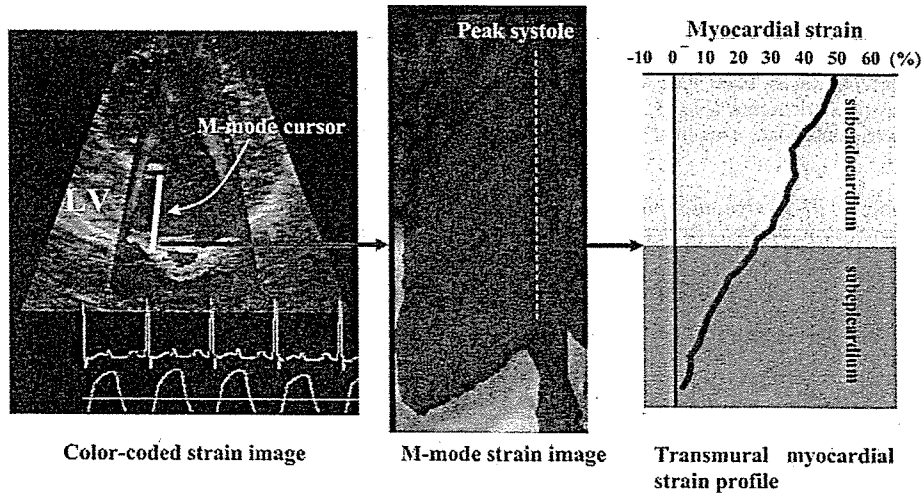

Fig. 2. Color-coded strain imaging, M-mode strain imaging, and transmural myocardial strain profile imaging in the control stage. *Left*: myocardial strain imaging of the left ventricular short axis at end systole. Red color means myocardial thickening. A white bar indicates an M-mode cursor. *Middle*: color-coded M-mode myocardial strain imaging obtained at the left ventricular posterior wall. The subendocardium is brighter than the subepicardium, indicating that the subendocardium contracts more vigorously. *Right*: transmural strain profile at end systole. The strain was highest at the subendocardium and lowest at the subepicardium, and the transmural strain showed a linear profile. LV, left ventricular wall.

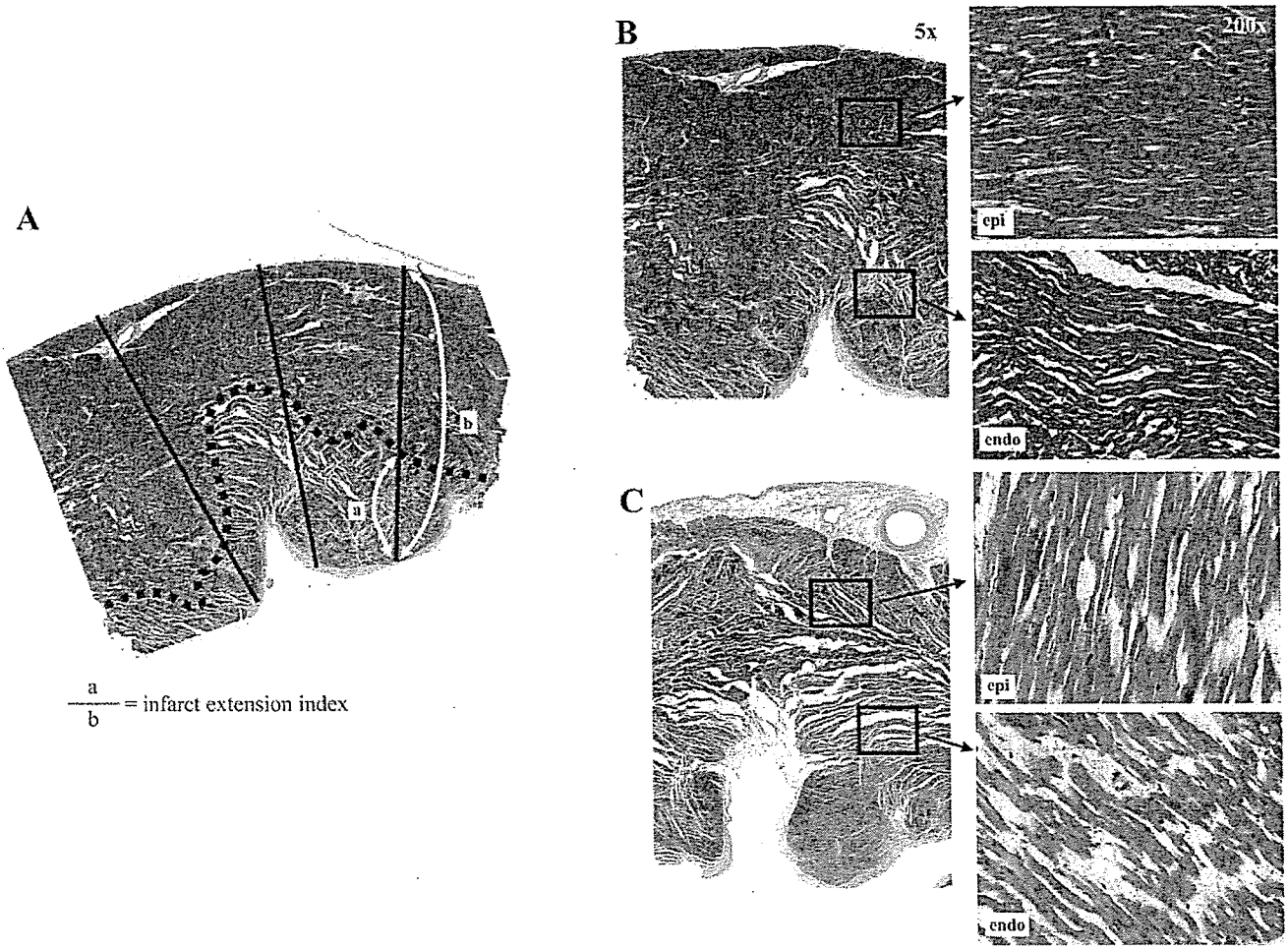

Fig. 3. *A*: determination of infarct extension index. Dotted line indicates the external limit of the infarcted zone. Examples of myocardial specimens taken after the SMI stage (*B*) and the TMI stage (*C*) stained by Masson's trichrome staining. In the SMI specimen, myocardial infarct was found only in the subendocardial layer, whereas acute ischemic changes such as wavy change or coagulation necrosis were recognized in both subendocardial and subepicardial layers in the TMI specimen. endo, Subendocardial layer; epi, subepicardial layer.

Histopathological studies. Establishment of subendocardial and transmural infarction by these techniques has been confirmed in our preliminary study and other previous studies (8, 10). We assessed the degree of extension of myocardial infarct also in the present study. At the end of the SMI stage in four dogs and the TMI stage in seven dogs, the heart was excised and cut into five to seven equally distant short-axis slices. Each slice was stained with hematoxylin-eosin and Masson's trichrome (Fig. 3). A pathologist who was blind to the experimental data examined the hearts histologically and measured the degree of infarct extension at the basal and midinferolateral walls, as previously reported (2). On each enlarged photomicrograph of the hearts, three to five transmural radii in the infarcted area were traced perpendicular to the endocardial and epicardial borders. The distance from the endocardial border to the external limit of the infarcted zone was measured and was expressed as a percentage of the distance between the endocardial and epicardial borders as an index of infarct extension, 100% being fully transmural and 0% being no infarction.

Table 1. *Hemodynamic parameters in control, SMI, and TMI stages*

	Baseline			DSE		
	Control (n = 13)	SMI (n = 11)	TMI (n = 7)	Control	SMI	TMI
HR, beats/min	133±17	128±27	129±27	149±22	134±27	150±19
LVP, mmHg	123±10*†	108±24	92±21	136±11†	132±28†	112±20
+dP/dt, mmHg/s	2,169±484*†‡	1,577±347*†	1,207±279*	4,021±979†‡	3,231±844†	2,478±1,138
−dP/dt, mmHg/s	−2,531±408*†	−1,824±606*†	−1,164±465*	−3,188±650†	−2,724±892	−2,104±526

Data are presented as means ± SD; n, no. of dogs. DSE, dobutamine stress echocardiography; SMI, subendocardial myocardial infarction; TMI, transmural myocardial infarction; HR, heart rate; LVP, peak systolic left ventricular pressure; +dP/dt, peak positive dP/dt; −dP/dt, peak negative dP/dt. $P < 0.05$ vs. DSE values (*), vs. SMI values (‡), and vs. TMI values (†).

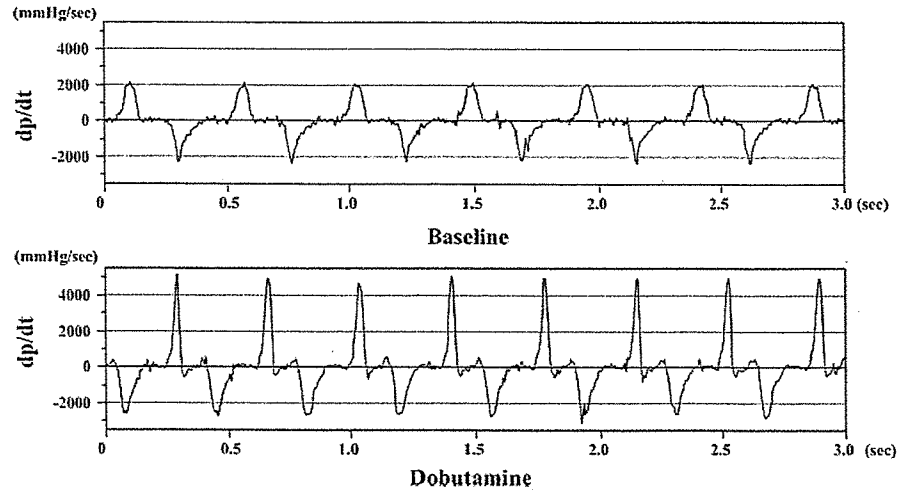

Fig. 4. dP/d*t* waveform before (*top*) and after (*bottom*) dobutamine infusion.

Reproducibility. Myocardial strain was measured by two independent observers and by one observer two times a week apart in 10 randomly selected segments to determine interobserver and intraobserver variability. The variability was assessed as the absolute difference between two measurements expressed as a percentage of their mean values. The interobserver variability was 6.5 ± 5.5 and 9.5 ± 7.5% for the subendocardial and subepicardial strains, respectively. The intraobserver variability was 7.2 ± 4.9 and 9.3 ± 3.7% for the subendocardial and subepicardial strains, respectively.

Statistical analysis. Hemodynamic data were obtained as an average of three to five consecutive beats. Statistical analyses were done with commercially available software (StatView 5.0; SAS Institute). Data are expressed as mean values ± SD. Comparisons of parameters among the stages were made by one-way ANOVA for repeated measures, followed by Scheffé's test. The Wilcoxon signed-ranks test was used to compare parameters before and after DSE. $P < 0.05$ was considered to indicate statistical significance.

RESULTS

Hemodynamic and histopathological data. Measurements were done in 13 dogs in the control stage, in 11 dogs in the SMI stage, and in 7 dogs in the TMI stage. Because of a large infarct created by the procedure, two dogs did not survive in the SMI stage and four dogs in the TMI stage. The absolute value of peak systolic left ventricular pressure and peak positive and negative dP/d*t* decreased gradually with the advancement of the stage. However, heart rate showed no significant changes. Both positive and negative dP/d*t* significantly increased in response to dobutamine administration (Table 1 and Fig. 4).

The degree of infarct extension was assessed at 14 sites from 4 dogs after the SMI stage and at 20 sites from 7 dogs after the TMI stage. The infarct extension index was 24.9 ± 7.8% for the SMI stage and 76.1 ± 9.9% for the TMI stage. Typical examples of the histopathological findings for both subendocardial and transmural infarcts are shown in Fig. 3.

Strain value in each stage. Myocardial strain was obtained at 25 segments in the control stage, at 20 segments in the SMI stage, and 11 segments in the TMI stage. Figure 5 shows representative TMSPs in each stage. In the control stage, myocardial strain was highest in the subendocardium and declined linearly toward the subepicardium. After DSE, TMSP

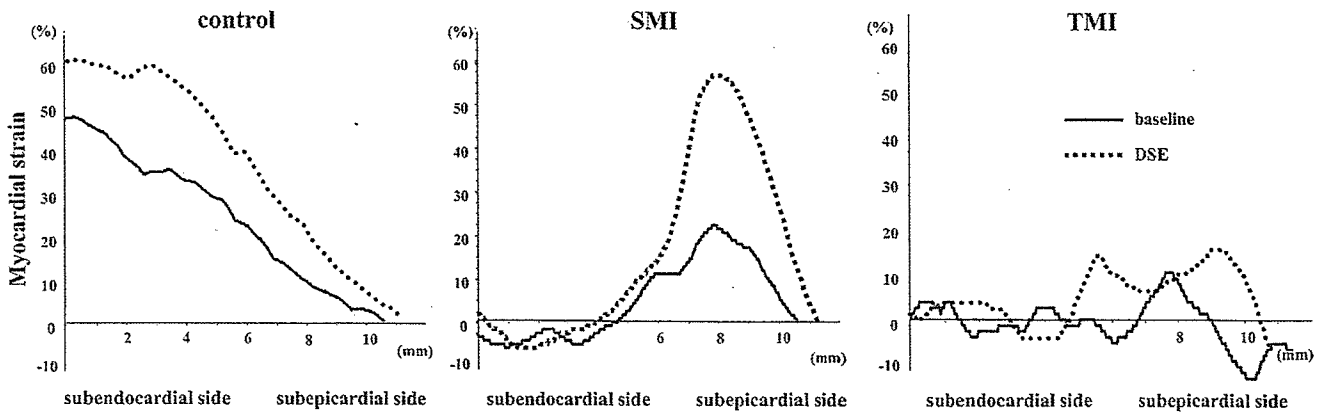

Fig. 5. Transmural myocardial strain profile before (solid lines) and after (dashed lines) dobutamine administration in each stage. *Left*: control stage. The profile was highest at the subendocardium and lowest at the subepicardium. With dobutamine administration, overall transmural myocardial strain increased. *Middle*: SMI stage. Myocardial strain at the subendocardium significantly decreased. With dobutamine administration, myocardial strain at the subepicardium showed a significant increase. *Right*: TMI stage. Overall transmural myocardial strain decreased at the baseline. Even after dobutamine administration, myocardial strain showed no significant increase.

Table 2. *Subendocardial and subepicardial strain in control, SMI, and TMI stages*

	Baseline			DSE		
	Control (n = 25)	SMI (n = 20)	TMI (n = 11)	Control	SMI	TMI
Endo strain	53.6±17.1*†‡	0.8±8.8	−3.9±5.6	73.3±21.8†‡	1.3±7.0	−1.9±6.0
Epi strain	23.9±6.1*†‡	12.4±7.3*†	−1.0±7.8	26.3±6.4†	27.1±8.8†	−0.7±8.3

Data are presented as means ± SD; n, no. of dogs. Endo strain, subendocardial strain; Epi strain, subepicardial strain. $P < 0.05$ vs. DSE values (*), vs. SMI values (‡), and vs. TMI values (†).

was uniformly uplifted, indicating the enhancement of contractility. In the SMI stage, subendocardial strain was almost zero before and after dobutamine challenge. In contrast, subepicardial strain increased after dobutamine, suggesting the presence of myocardial viability in the subepicardium. In the TMI stage, TMSP was almost flat before and after DSE, showing loss of myocardial viability through whole layers (Table 2).

Figure 6 shows changes in the subendocardial and subepicardial mean strain. Strain in the subendocardial half-layer was lower in the SMI and TMI stages than in the control stage (53.6 ± 17.1 vs. 0.8 ± 8.8 and −3.9 ± 5.6%, both $P < 0.001$).

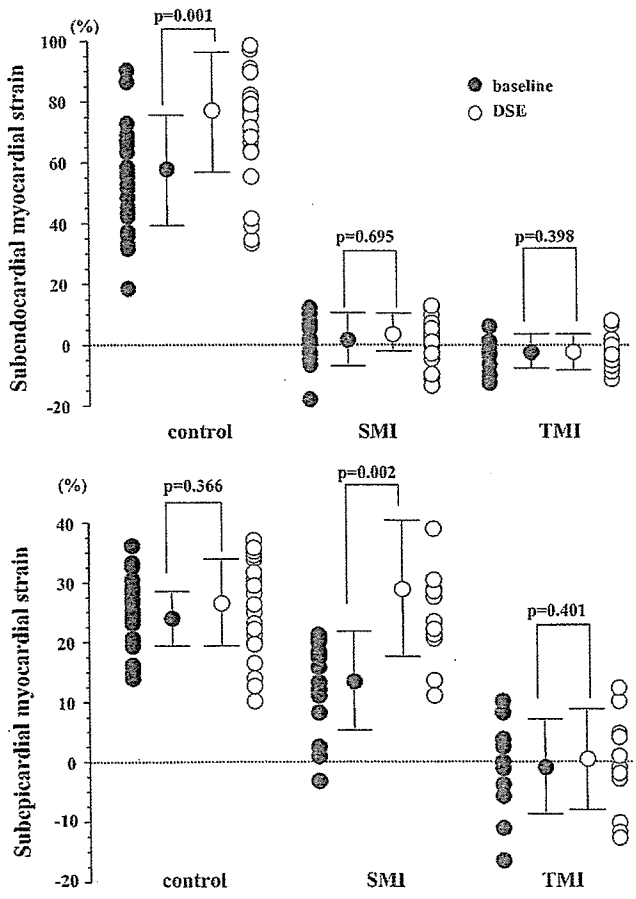

Fig. 6. Strain value in each layer. *Top*: subendocardial strain before (●) and after (○) dobutamine administration. Strain value in the subendocardial half-layer in the control stage increased with dobutamine, whereas that in the SMI and TMI stages showed no significant increase. *Bottom*: subepicardial strain before (●) and after (○) dobutamine administration. Strain value in the subepicardial half-layer in the SMI stage showed a significant increase. It showed no significant increase in the TMI stage.

There were no significant differences in the subendocardial strain between the SMI and TMI stages [P = not significant (NS)]. Strain in the subepicardial half-layer was lower in the TMI stage (−1.0 ± 7.8%) than that in the SMI stage (12.4 ± 7.3%, $P < 0.001$) and that in the control stage (23.9 ± 6.1%, $P < 0.001$).

Subendocardial strain in the control stage increased with DSE (53.6 ± 17.1 vs. 73.3 ± 21.8%, $P < 0.001$), whereas that in the SMI (0.8 ± 8.8 vs. 1.3 ± 7.0%, P = NS) and in the TMI stage (−3.9 ± 5.6 vs. −1.9 ± 6.0%, P = NS) showed no significant increase. Subepicardial strain in the control stage (23.9 ± 6.1 vs. 26.3 ± 6.4%, $P < 0.05$) and in the SMI stage (12.4 ± 7.3 vs. 27.1 ± 8.8%, $P < 0.005$) increased with DSE. It did not increase after DSE in the TMI stage (−1.0 ± 7.8 vs. −0.7 ± 8.3%, P = NS). Subepicardial strain after DSE showed no significant differences between the control and SMI stages (P = NS). These results showed that myocardial viability in the subepicardium was preserved in the SMI stage, whereas that in the TMI stage was lost.

DISCUSSION

In the present study, we analyzed the transmural distribution of viable muscle in myocardial infarction using echocardiography. Contraction in the subendocardium was lost and did not increase with dobutamine in either subendocardial infarction or transmural infarction models. On the other hand, subepicardial contraction was increased in subendocardial infarction but not in transmural infarction. These results showed that, with TMSP, we could quantify the transmural distribution of myocardial strain and identify the transmural differences in a local inotropic reserve in the viable and infarcted myocardium. The TMSP with DSE was useful to estimate the heterogeneity of transmural myocardial viability in SMI and TMI.

Transmural heterogeneity of myocardial viability. The left ventricular myocardium demonstrates transmural heterogeneity of strain distribution. It has been reported that, under normal circumstances, the subendocardial myocardium receives more blood flow and consumes more oxygen than the subepicardial one (20, 28, 35). Moreover, there is a transmural gradient of contractile function in the left ventricular wall, with greatest amount of thickening occurring in the subendocardial myocardium (6, 25). Clinically, these results were noninvasively confirmed in healthy subjects with tissue Doppler tracking technique (31). In the present study, strain value in the subendocardial layer was greater than that in the subepicardial layer in the control stage, being consistent with those of previous experimental and clinical studies. The linear decline pattern in TMSP was not observed in myocardial infarction. TMSP would potentially be useful for more detailed and innovative

evaluations of transmural myocardial function experimentally and clinically.

Effect of ischemia and dobutamine on transmural heterogeneity. After coronary artery occlusion, myocardial necrosis begins first in the endocardium and then progresses toward the epicardium with an increase in the occlusion time (8, 13). In our present study, we confirmed histologically that the SMI stage induced subendocardial infarction and the TMI stage induced transmural myocardial infarction. We observed continuous progression of myocardial dysfunction from the subendocardium to the subepicardium in myocardial infarction using echocardiography.

In acute animal models of reversible postischemic dysfunction and myocardial infarction, improved wall thickening during inotropic stimulation accurately differentiated reversible from fixed dysfunction and provided a better early assessment of viability than assessment of resting function alone (18). In clinical studies, contractile reserve by low-dose dobutamine was an independent predictor of functional recovery for myocardial infarction, which was superior to the other clinical criteria (23). In this experimental subendocardial infarction model, subendocardial strain showed no significant increase in response to inotropic stimulation, whereas subepicardial strain increased, indicating that the subepicardial myocardium was still viable. In the transmurally infarcted myocardium, myocardial strain of both subendocardium and subepicardium did not show significant increase. Therefore, the present method using TMSP and DSE is useful to visualize and quantify the contractile reserve and viability of both the subendocardium and the subepicardium.

Clinical implications. Because the prognosis of patients with subendocardial infarction is better than that with transmural infarction, assessment of the transmurality of myocardial necrosis and ischemia is an important clinical issue for patients with acute myocardial infarction or with chronic myocardial ischemia (22, 27). However, it has been difficult to make a diagnosis of subendocardial infarction by two-dimensional echocardiography. Some previous studies have shown that strain rate or strain echocardiography was useful to differentiate subendocardial infarction from transmural infarction (2, 34). We also obtained similar results using a new method of visualizing transmural myocardial strain distribution. Because the transmurality of necrosis is an important determinant of ultimate infarct size, its knowledge would be helpful in making therapeutic decisions for myocardial infarction (16, 34). Thus it is clinically helpful that we can quantify the transmural myocardial viability and necrosis extent. Furthermore, we could estimate the myocardial viability of each layer with DSE, enabling us to diagnose the stunned myocardium and predict myocardial functional recovery after myocardial infarction.

The present imaging system can be applied for the clinical evaluation of the various heart diseases characterized by subendocardial myocardial dysfunction such as anthracycline cardiotoxicity, syndrome X, hypertrophic cardiomyopathy, and dilated cardiomyopathy (14, 19, 21).

Study limitations. There was a possibility that some dogs in the subendocardial infarction models might develop transmural infarction. However, the 90-min ischemic period chosen for the subendocardial infarction models was similar to the previous studies, and it did result in subendocardial infarction (8, 10). In the present study, we showed histological evidence of subendocardial infarction after the SMI stage in parts of dogs. Furthermore, the difference in strain between the subendocardial and transmural infarction models was very prominent and consistent in each dog in the present study. These suggested that dogs after the SMI stage developed myocardial infarct almost only in the subendocardial layer.

We did not validate myocardial strain values using other methods, such as sonomicrometry. However, sonomicrometry is not always suitable to assess transmural distribution of myocardial strain, as shown in Fig. 5. We believe our measurement should be accurate because the displacement data obtained by our method were shown to be accurate (3, 21).

In conclusion, the quantitative analysis of transmural myocardial strain distribution could assess transmural differences in local inotropic reserve within the viable and infracted myocardium. In subendocardial infarction, the subepicardial myocardial strain showed an increase in contraction with dobutamine. However, in transmural infarction, this increase was lost. Assessment of transmural strain profile using tissue strain imaging was useful to quantify transmural distribution of the viable myocardium in SMI and TMI.

ACKNOWLEDGMENTS

We thank Yasuhiko Abe, Ryoichi Kanda, and Toshiba Corporation for providing research software assistance.

GRANTS

This work was partly supported by a Research Grant from the Ministry of Health, Labor and Welfare, Japan.

REFERENCES

1. **Chen X, Nakatani S, Hasegawa T, Maruo T, Kanzaki H, Miyatake K.** Effect of left ventricular systolic pressure on myocardial strain demonstrated by transmural myocardial strain profile. *Echocardiography* 23: 77–78, 2006.
2. **Derumeaux G, Loufoua J, Pontier G, Cribier A, Ovize M.** Tissue Doppler imaging differentiates transmural from nontransmural acute myocardial infarction after reperfusion therapy. *Circulation* 103: 589–596, 2001.
3. **Dohi K, Pinsky MR, Kanzaki H, Severyn D, Gorcsan J 3rd.** Effects of radial left ventricular dyssynchrony on cardiac performance using quantitative tissue Doppler radial strain imaging. *J Am Soc Echocardiogr* 19: 475–482, 2006.
4. **Edvardsen T, Gerber BL, Garot J, Bluemke DA, Lima JA, Smiseth OA.** Quantitative assessment of intrinsic regional myocardial deformation by Doppler strain rate echocardiography in humans: validation against three-dimensional tagged magnetic resonance imaging. *Circulation* 106: 50–56, 2002.
5. **Gallagher KP, Matsuzaki M, Koziol JA, Kemper WS, Ross J Jr.** Regional myocardial perfusion and wall thickening during ischemia in conscious dogs. *Am J Physiol Heart Circ Physiol* 247: H727–H738, 1984.
6. **Hartley CJ, Latson LA, Michael LH, Seidel CL, Lewis RM, Entman ML.** Doppler measurement of myocardial thickening with a single epicardial transducer. *Am J Physiol Heart Circ Physiol* 245: H1066–H1072, 1983.
7. **He KL, Dickstein M, Sabbah HN, Yi GH, Gu A, Maurer M, Wei CM, Wang J, Burkhoff D.** Mechanisms of heart failure with well preserved ejection fraction in dogs following limited coronary microembolization. *Cardiovasc Res* 64: 72–83, 2004.
8. **Homans DC, Pavek T, Laxson DD, Bache RJ.** Recovery of transmural and subepicardial wall thickening after subendocardial infarction. *J Am Coll Cardiol* 24: 1109–1116, 1994.
9. **Jamal F, Strotmann J, Weidemann F, Kukulski T, D'hooge J, Bijnens B, Van de Werf F, De Scheerder I, Sutherland GR.** Noninvasive quantification of the contractile reserve of stunned myocardium by ultrasonic strain rate and strain. *Circulation* 104: 1059–1065, 2001.
10. **Kim WG, Shin YC, Hwang SW, Lee C, Na CY.** Comparison of myocardial infarction with sequential ligation of the left anterior descend-

ing artery and its diagonal branch in dogs and sheep. *Int J Artif Organs* 26: 351–357, 2003.

11. **Kukulski T, Jamal F, Herbots L, D'hooge J, Bijnens B, Hatle L, De Scheerder I, Sutherland GR.** Identification of acutely ischemic myocardium using ultrasonic strain measurements. A clinical study in patients undergoing coronary angioplasty. *J Am Coll Cardiol* 41: 810–819, 2003.
12. **Lavine SJ, Prcevski P, Held AC, Johnson V.** Experimental model of chronic global left ventricular dysfunction secondary to left coronary microembolization. *J Am Coll Cardiol* 18: 1794–1803, 1991.
13. **Lowe JE, Cummings RG, Adams DH, Hull-Ryde EA.** Evidence that ischemic cell death begins in the subendocardium independent of variations in collateral flow or wall tension. *Circulation* 68: 190–202, 1983.
14. **Maier SE, Fischer SE, McKinnon GC, Hess OM, Krayenbuehl HP, Boesiger P.** Evaluation of left ventricular segmental wall motion in hypertrophic cardiomyopathy with myocardial tagging. *Circulation* 86: 1919–1928, 1992.
15. **Malyar NM, Lerman LO, Gossl M, Beighley PE, Ritman EL.** Relation of nonperfused myocardial volume and surface area to left ventricular performance in coronary microembolization. *Circulation* 110: 1946–1952, 2004.
16. **Mann DL, Gillam LD, Mich R, Foale R, Newell JB, Weyman AE.** Functional relation between infarct thickness and regional systolic function in the acutely and subacutely infarcted canine left ventricle. *J Am Coll Cardiol* 14: 481–488, 1989.
17. **Matre K, Fannelop T, Dahle GO, Heimdal A, Grong K.** Radial strain gradient across the normal myocardial wall in open-chest pigs measured with Doppler strain rate imaging. *J Am Soc Echocardiogr* 18: 1066–1073, 2005.
18. **Mercier JC, Lando U, Kanmatsuse K, Ninomiya K, Meerbaum S, Fishbein MC, Swan HJ, Ganz W.** Divergent effects of inotropic stimulation on the ischemic and severely depressed reperfused myocardium. *Circulation* 66: 397–400, 1982.
19. **Mortensen SA, Olsen HS, Baandrup U.** Chronic anthracycline cardiotoxicity: haemodynamic and histopathological manifestations suggesting a restrictive endomyocardial disease. *Br Heart J* 55: 274–282, 1986.
20. **Oh BH, Volpini M, Kambayashi M, Murata K, Rockman HA, Kassab GS, Ross J Jr.** Myocardial function and transmural blood flow during coronary venous retroperfusion in pigs. *Circulation* 86: 1265–1279, 1992.
21. **Panting JR, Gatehouse PD, Yang GZ, Grothues F, Firmin DN, Collins P, Pennell DJ.** Abnormal subendocardial perfusion in cardiac syndrome X detected by cardiovascular magnetic resonance imaging. *N Engl J Med* 346: 1948–1953, 2002.
22. **Picano E, Sicari R, Landi P, Cortigiani L, Bigi R, Coletta C, Galati A, Heyman J, Mattioli R, Previtali M, Mathias W Jr, Dodi C, Minardi G, Lowenstein J, Seveso G, Pingitore A, Salustri A, Raciti M.** Prognostic value of myocardial viability in medically treated patients with global left ventricular dysfunction early after an acute uncomplicated myocardial infarction: a dobutamine stress echocardiographic study. *Circulation* 98: 1078–1084, 1998.
23. **Pierard LA, De Landsheere CM, Berthe C, Rigo P, Kulbertus HE.** Identification of viable myocardium by echocardiography during dobutamine infusion in patients with myocardial infarction after thrombolytic therapy: comparison with positron emission tomography. *J Am Coll Cardiol* 15: 1021–1031, 1990.
24. **Pislaru C, Bruce CJ, Anagnostopoulos PC, Allen JL, Seward JB, Pellikka PA, Ritman EL, Greenleaf JF.** Ultrasound strain imaging of altered myocardial stiffness: stunned versus infarcted reperfused myocardium. *Circulation* 109: 2905–2910, 2004.
25. **Sabbah HN, Marzilli M, Stein PD.** The relative role of subendocardium and subepicardium in left ventricular mechanics. *Am J Physiol Heart Circ Physiol* 240: H920–H926, 1981.
26. **Sade LE, Severyn DA, Kanzaki H, Dohi K, Gorcsan J 3rd.** Second-generation tissue Doppler with angle-corrected color-coded wall displacement for quantitative assessment of regional left ventricular function. *Am J Cardiol* 92: 554–560, 2003.
27. **Sawada S, Bapat A, Vaz D, Weksler J, Fineberg N, Greene A, Gradus-Pizlo I, Feigenbaum H.** Incremental value of myocardial viability for prediction of long-term prognosis in surgically revascularized patients with left ventricular dysfunction. *J Am Coll Cardiol* 42: 2099–2105, 2003.
28. **Sjoquist PO, Duker G, Almgren O.** Distribution of the collateral blood flow at the lateral border of the ischemic myocardium after acute coronary occlusion in the pig and the dog. *Basic Res Cardiol* 79: 164–175, 1984.
29. **Skulstad H, Urheim S, Edvardsen T, Andersen K, Lyseggen E, Vartdal T, Ihlen H, Smiseth OA.** Grading of myocardial dysfunction by tissue Doppler echocardiography: a comparison between velocity, displacement, and strain imaging in acute ischemia. *J Am Coll Cardiol* 47: 1672–1682, 2006.
30. **Tanaka N, Tone T, Ono S, Tomochika Y, Murata K, Kawagishi T, Yamazaki N, Matsuzaki M.** Predominant inner-half wall thickening of left ventricle is attenuated in dilated cardiomyopathy: an application of tissue Doppler tracking technique. *J Am Soc Echocardiogr* 14: 97–103, 2001.
31. **Torry RJ, Myers JH, Adler AL, Liut CL, Gallagher KP.** Effects of nontransmural ischemia on inner and outer wall thickening in the canine left ventricle. *Am Heart J* 122: 1292–1299, 1991.
32. **Uematsu M, Miyatake K, Tanaka N, Matsuda H, Sano A, Yamazaki N, Hirama M, Yamagishi M.** Myocardial velocity gradient as a new indicator of regional left ventricular contraction: detection by a two-dimensional tissue Doppler imaging technique. *J Am Coll Cardiol* 26: 217–223, 1995.
33. **Urheim S, Edvardsen T, Torp H, Angelsen B, Smiseth OA.** Myocardial strain by Doppler echocardiography. Validation of a new method to quantify regional myocardial function. *Circulation* 102: 1158–1164, 2000.
34. **Weidemann F, Dommke C, Bijnens B, Claus P, D'hooge J, Mertens P, Verbeken E, Maes A, Van de Werf F, De Scheerder I, Sutherland GR.** Defining the transmurality of a chronic myocardial infarction by ultrasonic strain-rate imaging: implications for identifying intramural viability: an experimental study. *Circulation* 107: 883–888, 2003.
35. **Weiss HR, Neubauer JA, Lipp JA, Sinha AK.** Quantitative determination of regional oxygen consumption in the dog heart. *Circ Res* 42: 394–401, 1978.
36. **Williams RI, Payne N, Phillips T, D'hooge J, Fraser AG.** Strain rate imaging after dynamic stress provides objective evidence of persistent regional myocardial dysfunction in ischaemic myocardium: regional stunning identified? *Heart* 91: 152–160, 2005.

REGULAR PAPER

J. Physiol. Sci. Vol. 56, No. 5 Oct. 2006; pp. 325–333
Online Sep. 9, 2006; **doi:10.2170/physiolsci.RP009006**

Baroreflex Increases Correlation and Coherence of Muscle Sympathetic Nerve Activity (SNA) with Renal and Cardiac SNAs

Atsunori KAMIYA, Toru KAWADA, Masaki MIZUNO, Tadayoshi MIYAMOTO, Kazunori UEMURA, Kenjiro SEKI, Shuji SHIMIZU, and Masaru SUGIMACHI

Department of Cardiovascular Dynamics, National Cardiovascular Centre Research Institute, Osaka, 565-8565 Japan

Reprinted from
The Journal of Physiological Sciences
Volume 56, Number 5, pp. 325–333, 2006
http://jphysiol.umin.jp doi:10.2170/physiolsci.RP009006

Published by The Physiological Society of Japan

Received on Jul 27, 2006; accepted on Sep 6, 2006; released online on Sep 9, 2006; doi:10.2170/physiolsci.RP009006
Correspondence should be addressed to: Atsunori Kamiya, Department of Cardiovascular Dynamics, National Cardiovascular Centre Research Institute, Osaka 565-8565, Japan. Tel: +81-6-6833-5012; Fax: +81-6-6835-5403; E-mail: kamiya@ri.ncvc.go.jp

REGULAR PAPER

J. Physiol. Sci. Vol. 56, No. 5; Oct. 2006; pp. 325–333
Online Sep. 9, 2006; **doi:10.2170/physiolsci.RP009006**

Baroreflex Increases Correlation and Coherence of Muscle Sympathetic Nerve Activity (SNA) with Renal and Cardiac SNAs

Atsunori KAMIYA, Toru KAWADA, Masaki MIZUNO, Tadayoshi MIYAMOTO, Kazunori UEMURA, Kenjiro SEKI, Shuji SHIMIZU, and Masaru SUGIMACHI

Department of Cardiovascular Dynamics, National Cardiovascular Centre Research Institute, Osaka, 565-8565 Japan

Abstract: Despite accumulating data of muscle sympathetic nerve activity (SNA) measured by human microneurography, whether neural discharges of muscle SNA correlates and coheres with those of other SNAs controlling visceral organs remains unclear. Further, how the baroreflex control of SNA affects the relations between these SNAs remains unknown. In urethane and α-chloralose anesthetized, vagotomized, and aortic-denervated rabbits, we recorded muscle SNA from the tibial nerve using microneurography and simultaneously recorded renal and cardiac SNAs. After isolating the carotid sinuses, we produced a baroreflex closed-loop condition by matching the isolated intracarotid sinus pressure (CSP) with systemic arterial pressure (CLOSE). We also fixed CSP at operating pressure (FIX) or altered CSP widely (WIDE: operating pressure ± 40 mmHg). Under these conditions, we calculated time-domain and frequency-domain measures of the correlation between muscle SNA and renal or cardiac SNAs. At CLOSE, muscle SNA resampled at 1 Hz correlated with both renal ($r^2 = 0.71 \pm 0.04$, delay = 0.10 ± 0.004 s) and cardiac SNAs ($r^2 = 0.58 \pm 0.03$, delay = 0.13 ± 0.004 s) at optimal delays. Moreover,muscle SNA at CLOSE strongly cohered with renal and cardiac SNAs(coherence >0.8) at the autospectral peak frequencies, and weakly (0.4–0.5) at the remaining frequencies. Increasing the magnitude of CSP change from FIX to CLOSE and further to WIDE resulted in corresponding increases in correlation and coherence functions at nonpeak frequencies, and the coherence functions at peak frequencies remained high (>0.8). In conclusion, muscle SNA correlates and coheres approximately with renal and cardiac SNAs under closed-loop baroreflex conditions. The arterial baroreflex is capable of potently homogenizing neural discharges of these SNAs by modulating SNA at the nonpeak frequencies of SNA autospectra.

Key words: sympathetic nerve activity, muscle, baroreflex.

Sympathetic nerve activity (SNA) has the crucial role of controlling circulation [1] and thus has been a major target in the research of circulatory physiology and pathophysiology. In humans, microneurography is the only direct method to measure SNA discharge [2]. By this technique, numerous human studies measured the activity of sympathetic nerves innervating the blood vessels in skeletal muscles (muscle SNA) [2–5] and used it as systemic SNA [3, 6–10]. However, since the measurable region in humans by this technique is almost limited to upper and lower extremities [2], the relation between muscle SNA and the SNAs controlling visceral organs such as the kidney and heart is not fully understood.

Arterial baroreflex is a major controller of SNA and thus may affect the relations between these SNAs. We previously reported that static-nonlinear and dynamic-linear baroreflex control of muscle SNA is similar to that of renal and cardiac SNAs under physiological pressure change in rabbits [11, 12]. Consistent with this finding, we have indeed observed that muscle SNA averaged over 1 minute parallels renal and cardiac SNAs in response to forced baroreceptor pressure change [11]. However, the relation between these SNAs in a time domain faster than 1 min and the relation in frequency domain remain unknown, despite the importance of their physiological and clinical relevance. First, the relation between these SNAs under conditions in which arterial pressure is regulated to normal level by a closed-loop baroreflex system is unclear. Next, the effects of baroreflex on the homogeneity in SNAs have not been analyzed quantitatively. Although canceling and enlarging the changes in baroreceptor pressure under open-loop baroreflex conditions are speculated to decrease and increase the homogeneity, respectively, how much muscle SNA correlates and coheres with other SNAs under these conditions remains unknown.

In the present study, we tested two hypotheses: (i) muscle SNA correlates and coheres with renal and cardiac SNAs under a closed-loop baroreflex condition, and (ii) the arterial baroreflex is capable of homogenizing neural discharges of these SNAs. In anesthetized rabbits with ca-

Received on Jul 27, 2006; accepted on Sep 6, 2006; released online on Sep 9, 2006; doi:10.2170/physiolsci.RP009006
Correspondence should be addressed to: Atsunori Kamiya, Department of Cardiovascular Dynamics, National Cardiovascular Centre Research Institute, Osaka 565-8565, Japan. Tel: +81-6-6833-5012; Fax: +81-6-6835-5403; E-mail: kamiya@ri.ncvc.go.jp

rotid sinuses isolated from systemic circulation, we simultaneously recorded muscle SNA from the tibial nerve by microneurography as well as renal and cardiac SNAs. We investigated the relation of muscle SNA with renal and cardiac SNAs under closed-loop baroreflex conditions and determined the proportions of the variance components of muscle SNA correlating and not correlating with renal and cardiac SNAs. Further, we also investigated these relations under two open-loop baroreflex conditions: fixed and widely fluctuating baroreceptor pressure.

MATERIALS AND METHODS

Surgical preparations. The animals were cared for in strict accordance with the Guiding Principles for the Care and Use of Animals in the Field of Physiological Sciences approved by the Physiological Society of Japan. Ten Japanese white rabbits weighing 2.4–3.3 kg were anesthetized by intravenous injection (2 ml/kg) of a mixture of urethane (250 mg/ml) and α-chloralose (40 mg/ml) and mechanically ventilated with oxygen-enriched room air. Supplemental anesthetics were injected as necessary (0.5 ml/kg) to maintain an appropriate level of anesthesia. We isolated the bilateral carotid sinuses vascularly from the systemic circulation by ligating the internal and external carotid arteries and other small branches originating from the carotid sinus regions. The isolated carotid sinuses were filled with warmed physiological saline through catheters inserted via the common carotid arteries. The intracarotid sinus pressure (CSP) was controlled by a servo-controlled piston pump (model ET-126A, Labworks; Costa Mesa, CA). Bilateral vagal and aortic depressor nerves were sectioned at the midlevel of the neck to eliminate baroreflexes from the cardiopulmonary region and the aortic arch. The systemic arterial pressure (AP) was measured using a high-fidelity pressure transducer (Millar Instruments; Houston, TX) inserted retrograde from the right common carotid artery below the isolated carotid sinus region. Body temperature was maintained at approximately 38°C with a heating pad.

We exposed the left renal sympathetic nerve retroperitoneally and the left cardiac sympathetic nerve through a middle thoracotomy. We attached a pair of stainless steel wire electrodes (Bioflex wire AS633, Cooner Wire) to each of these nerves to record renal and cardiac SNAs. To eliminate afferent signals, we tightly ligated and crushed the nerve fibers peripheral to the electrodes. To insulate and fix the electrodes, we covered the nerve and electrodes with a mixture of silicone gel (Silicon Low Viscosity, KWIK-SIL, World Precision Instrument, Inc., FL). We band-pass filtered the preamplified nerve signals at 150–1,000 Hz.

We exposed the left tibial nerve at the right popliteal fossa by incising the flexors of the dorsal middle thigh. We inserted a tungsten microelectrode (model 26-05-1, Federick Haer and Co., Bowdoinham, ME) to the right tibial nerve to record muscle SNA according to the microneurographic technique reported in humans [2, 13] and animals [14]. We identified muscle SNA according to the following discharge characteristics: (i) afferent activity being induced by tapping of the calf muscles but not by gently touching the skin, and (ii) excitatory and inhibitory responses to decreasing and increasing CSP, respectively. Then we tightly ligated and crushed the nerve fibers peripheral to the electrodes to eliminate afferent signals from the muscles. We fed the nerve signals into a preamplifier (Kohno Instruments, Nagoya) with active band-pass filters set from 480 to 5,000 Hz and continuously monitored these signals through a sound speaker.

We full-wave rectified and low-pass filtered the SNA signals with a cutoff frequency of 30 Hz to quantify the nerve activity. Pancuronium bromide (0.1 mg/kg) was administrated to prevent a contamination of muscular activity in these SNA recordings.

Protocols. After the surgical preparation, we kept the animal horizontally in a supine position. To test the first hypothesis that a neural discharge of muscle SNA parallels that of renal and cardiac SNAs, we measured the three SNAs while closing the baroreflex negative feedback loop by matching CSP with systemic AP (CLOSE protocol). We recorded CSP, SNAs, and systemic AP for 15 min at a sampling rate of 200 Hz, using a 12-bit analog-to-digital converter. After stabilizing the condition for at least 5 min, we recorded the data for 10 min and stored them on the hard disk of a dedicated laboratory computer system for later analysis. We also calculated the actual operating pressure by averaging systemic AP from the data.

To test the second hypothesis that baroreflex contributes to homogeneous sympathetic activation, we eliminated and greatly widened the baroreceptor pressure changes by the FIX and WIDE protocols, respectively, in baroreflex open-loop conditions. In the FIX protocol, we fixed CSP at the operating pressure [15, 16]. In the WIDE protocol, we randomly assigned CSP at 40 mmHg either above or below the operating pressure every 500 ms according to a binary white noise sequence [15, 17], where the input power spectrum of CSP was reasonably flat up to 1 Hz. The FIX and WIDE protocols were conducted serially in a randomized order at intervals of at least 5 min between protocols. During each protocol, we recorded measurements for 10 min and stored the data for analysis.

Data analysis. Under each baroreceptor pressure condition of CLOSE, WIDE, and FIX, we calculated the time domain (correlation coefficient) and frequency domain measures (coherence function) between muscle and renal or cardiac SNAs. In the time-domain analysis, we resampled SNA data at 1 Hz, assigned 100 arbitrary units (a.u.) to the maximal value during 10 min of CLOSE, and normalized other SNA signals to this value.

We scatter-plotted muscle SNA at 1 Hz against renal and cardiac SNAs with variable delays from renal and cardiac SNAs to muscle SNA (range: from 0 to 0.30 s at increments of 0.01 s) and calculated the correlation coefficient (r) [18] with optimal delays that maximized the square of correlation coefficient (r^2). The delays reflected the distances from the brain to the sites of measurement of these SNAs. The r^2 shows how perfectly a linear regression line describes the relationship between the two SNAs [19].

We also calculated the variance of muscle SNA resampled at 1 Hz [19]. The variance may include two components, one that correlates (correlative variance) and the other that does not correlate (noncorrelative variance) with other SNAs. Therefore we defined correlative and noncorrelative variance of muscle SNA to renal or cardiac SNA as follows (see APPENDIX) [18, 19]:

Correlative variance = SNA variance·r^2

Noncorrelative variance = SNA variance·$(1 - r^2)$

where SNA variance was the variance of muscle SNA, and r^2 was the correlation coefficient of muscle SNA against renal or cardiac SNA.

In the frequency-domain analysis, we calculated the coherence functions between muscle SNA and renal or cardiac SNA. We resampled SNA data at 10 Hz, and segmented them into 10 sets of 50% overlapping bins of 2^{10} data point each. SNA signals were similarly normalized as mentioned above. The segment length was 102.4 s, which yields the lowest frequency bound of 0.01 (0.0097) Hz. For each data set, we performed a fast Fourier transform while subtracting a linear trend and applying a Hanning window for each segment. We performed fast Fourier transform and ensemble averaged the power of muscle SNA [$S_{xx}(f)$], the power of renal or cardiac SNA [$S_{yy}(f)$], and the cross power between muscle SNA and renal or cardiac SNA [$S_{yx}(f)$] over the 10 segments. We derived a magnitude-squared coherence function [$Coh(f)$] of muscle SNA versus renal and cardiac SNAs as follows [17]:

$$Coh(f) = \frac{|S_{yx}(f)|^2}{S_{xx}(f)S_{yy}(f)}$$

The coherence value ranges from zero to unity. Unity coherence indicates a perfect linear correlation between muscle SNA and other SNAs, whereas zero coherence indicates total independence of the two SNAs. In an SNA autospectrum, when the power was three times greater than the averaged power of SNA from 0.01 to 1 Hz, we defined it as a peak. We separately calculated the averaged coherence function at the peak frequencies of muscle SNA autospectra and that at the remaining frequencies.

Statistic analysis. We presented all data as means ± SD. We used a repeated-measures analysis of variance with post hoc multiple comparisons to compare variables among experimental baroreceptor pressure conditions (FIX, CLOSE, WIDE) [19]. We considered differences significant when $P < 0.05$.

RESULTS

Relation between muscle SNA and cardiac or renal SNA in closed-loop baroreflex condition of CLOSE protocol

Time-domain analysis. In the CLOSE protocol (CSP matched with systemic arterial pressure), typical neural discharges of muscle SNA at 10 Hz appeared roughly the same as those of renal and cardiac SNAs (Fig. 1A). When the delay from renal and cardiac SNAs to muscle SNA was determined in individual animals to maximize r^2 (a typical example is shown in Fig. 1), muscle SNA resampled at 1 Hz correlated with both renal and cardiac SNAs with r^2 of 0.81 (delay = 0.10 s) and 0.64 (delay = 0.13 s), respectively (Fig. 1, B and C). The averaged data of all animals also showed that muscle SNA correlated with renal SNA ($r^2 = 0.71 \pm 0.04$, delay = 0.10 ± 0.004 s) and with

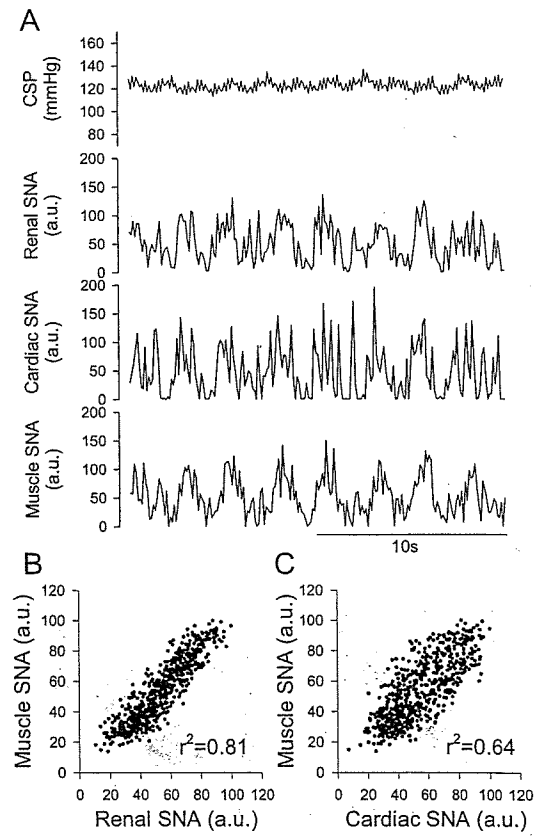

Fig. 1. (**A**) Representative time series for CSP, renal, cardiac, and muscle SNAs resampled at 10 Hz under the baroreflex closed-loop condition of CLOSE (CSP was matched to systemic AP). (**B**) Scatter plot of muscle SNA against renal SNA. (**C**) Scatter plot of muscle SNA against cardiac SNAs. The SNA signals were further resampled at 1 Hz. The delay from renal (0.10 s) or cardiac SNA (0.13 s) to muscle SNA was determined as the value that maximized r^2.

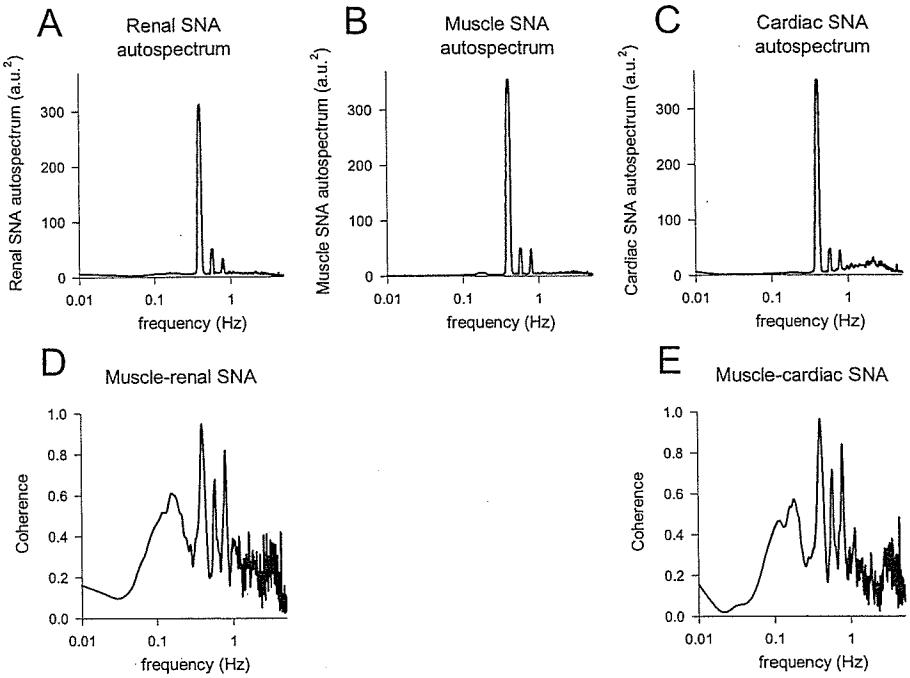

Fig. 2. Autospectra of renal (**A**), muscle (**B**), and cardiac SNAs (**C**) resampled at 1 Hz, and the coherence function of muscle SNA against renal (**D**) and cardiac SNAs (**E**) under the baroreflex closed-loop condition of CLOSE (CSP was matched to systemic AP), using the same data as in Fig. 1.

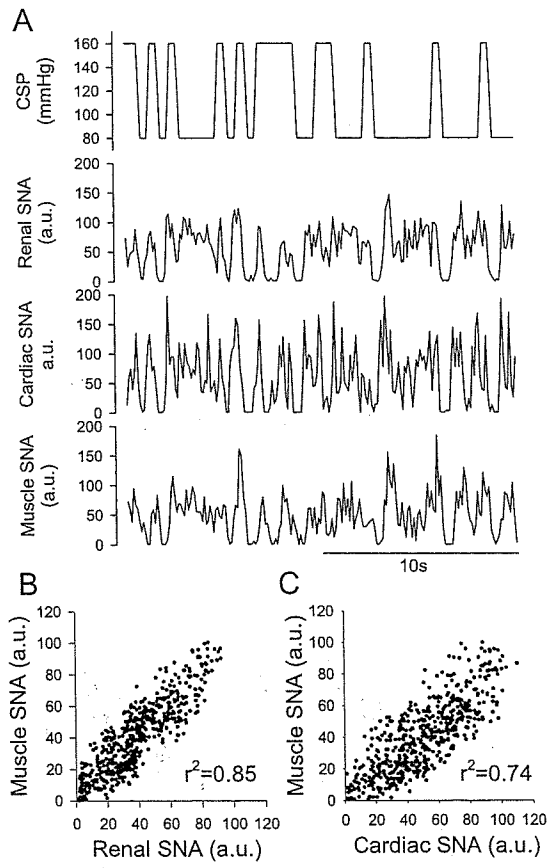

Fig. 3. (**A**) Representative time series for CSP, renal, cardiac, and muscle SNAs resampled at 10 Hz under the baroreflex open-loop condition of WIDE (CSP was varied according to a binary white noise sequence at 40 mmHg either above or below the operating pressure). (**B**) Scatter plots of muscle SNA resampled at 1 Hz against renal SNA (delay = 0.10 s). (**C**) Scatter plots of muscle SNA resampled at 1 Hz against cardiac SNA (delay = 0.13 s).

cardiac SNA (r^2 = 0.58 ± 0.03, delay = 0.13 ± 0.004 s) (Fig. 5, A and B). The r^2 was greater with renal than with cardiac SNA ($P < 0.05$). The pulse pressure of CSP was 30–40 mmHg.

Frequency-domain analysis. In the same animal as in Fig. 1, the autospectra of these SNAs showed a few peaks at common frequency ranges (Fig. 2, A, B, and C). Muscle SNA cohered with both renal and cardiac SNAs strongly at the peak frequencies of muscle SNA autospectra, but weakly at the remaining frequencies (Fig. 2, D and E). The individual animals all showed similar characteristics. The averaged coherence function of the animals was strong at the peak frequencies of the muscle SNA autospectrum (0.93 ± 0.01 between muscle and renal SNAs and 0.87 ± 0.02 between muscle and cardiac SNAs), but was weak at the remaining frequencies (0.5) (Fig. 8).

Effects of the magnitude of change in baroreceptor pressure on the relation between muscle SNA and cardiac or renal SNA

Time-domain analysis. In the same animal as in Fig. 1, the pattern of neural discharge of muscle SNA at 10 Hz resembled those of renal and cardiac SNAs to a greater extent in the WIDE protocol (CPS fluctuating between operating pressure ± 40 mmHg) (Fig. 3) than in the FIX protocol (CPS fixed at operating pressure) (Fig. 4). The correlation of muscle SNA resampled at 1 Hz with renal and cardiac SNAs was higher in WIDE (r^2 = 0.85, delay = 0.10 s, and r^2 = 0.74, delay = 0.13 s, respectively) (Fig. 3, B and C) than in CLOSE, but was lower in FIX (with the same delays, Fig. 4, B and C). Compared with CLOSE, the averaged data of all animals showed a higher correlation of muscle SNA with renal and cardiac SNAs in WIDE (r^2 = 0.79 ± 0.03, delay = 0.10 ± 0.004 s, and r^2 =

0.76 ± 0.02, delay = 0.13 ± 0.004 s, respectively), but lower correlation in FIX (r^2 = 0.53 ± 0.04, delay = 0.10 ± 0.004 s, and r^2 = 0.46 ± 0.04, delay = 0.13 ± 0.004 s, respectively) (Fig. 5, A and B). In WIDE, the r^2 was higher with renal than with cardiac SNA ($P < 0.05$). Similar results were observed when SNAs were resampled at slower and faster frequencies than 1 Hz (Fig. 6). In both SNA pairs, the r^2 was greater in WIDE than in CLOSE and FIX at frequencies from 0.01 to 5 Hz ($P < 0.05$), whereas it was greater in CLOSE than in FIX at frequencies from 0.3 to 5 Hz ($P < 0.05$).

The variance of muscle SNA sampled at 1 Hz increased from FIX to CLOSE and further to WIDE (Fig. 5, C and D; gray plus black column). The variance component of

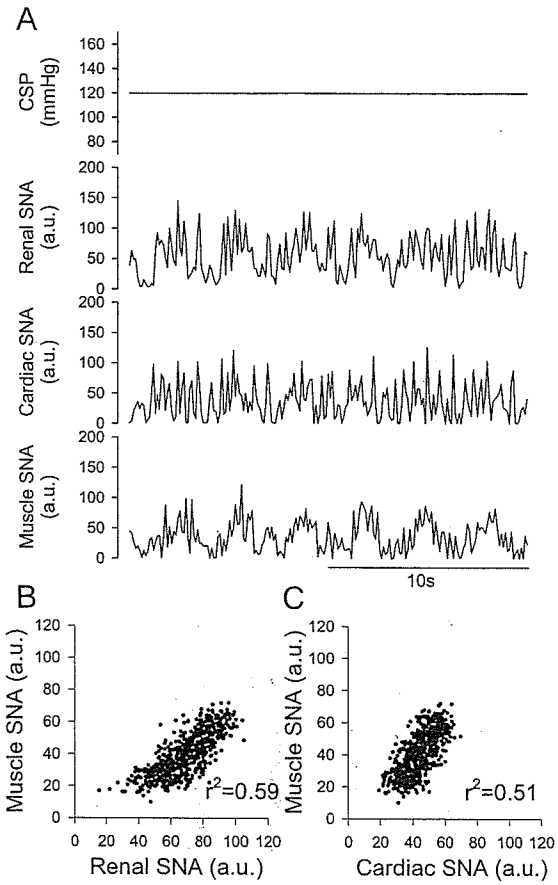

Fig. 4. (**A**) Representative time series for CSP, renal, cardiac, and muscle SNAs resampled at 10 Hz under the baroreflex open-loop condition of FIX (CSP was fixed at the operating pressure). (**B**) Scatter plot of muscle SNA resampled at 1 Hz against renal SNA (delay = 0.10 s). (**C**) Scatter plots of muscle SNA resampled at 1 Hz against cardiac SNA (delay = 0.13 s).

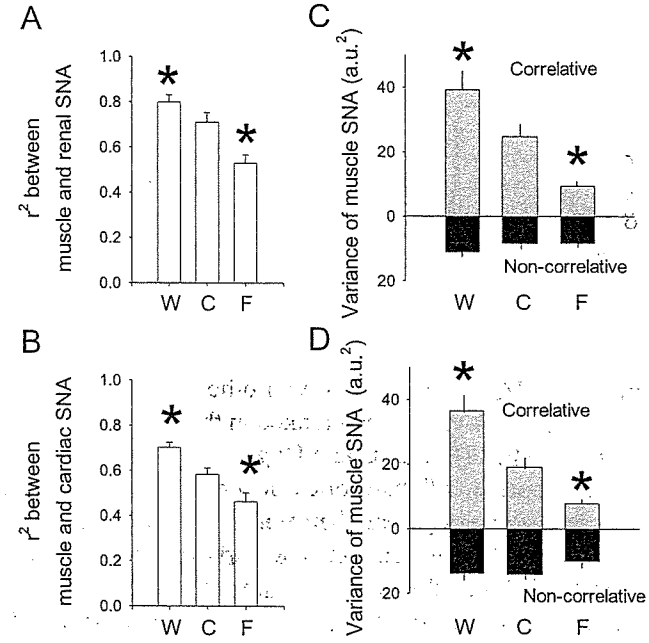

Fig. 5. The square of correlation coefficient (r^2) between muscle SNA resampled at 1 Hz and renal (**A**) or cardiac SNA (**B**) under baroreceptor pressure conditions of WIDE, CLOSE, and FIX. Floating columns show the averaged (±SD) correlative (gray top column) and noncorrelative (black bottom column) variance of muscle SNA versus renal (**C**) or cardiac SNA (**D**) resampled at 1 Hz in WIDE, CLOSE, and FIX. Correlative: variance component of muscle SNA correlating with other SNA; Noncorrelative: variance component of muscle SNA not correlating with other SNA; W: WIDE; C: CLOSE; F: FIX. *: $P < 0.05$, vs. CLOSE.

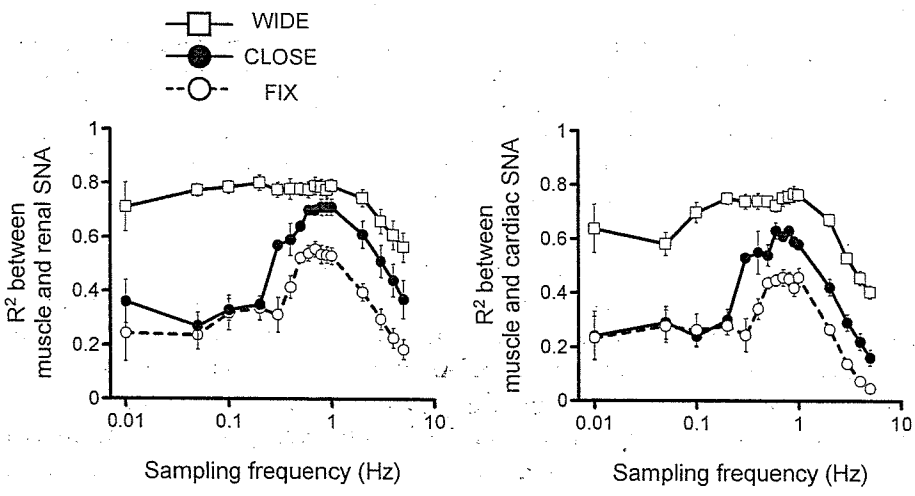

Fig. 6. The square of correlation coefficient (r^2) over SNA sampling frequency (0.01–5.0 Hz) between muscle SNA and renal (**A**) or cardiac SNA (**B**) under baroreceptor pressure conditions of WIDE (open square), CLOSE (closed circle), and FIX (open circle). In both SNA pairs, the r^2 was greater in WIDE than in CLOSE and FIX at frequencies observed ($P < 0.05$), whereas it was greater in CLOSE than in FIX at frequencies from 0.3 to 5.0 Hz ($P < 0.05$).

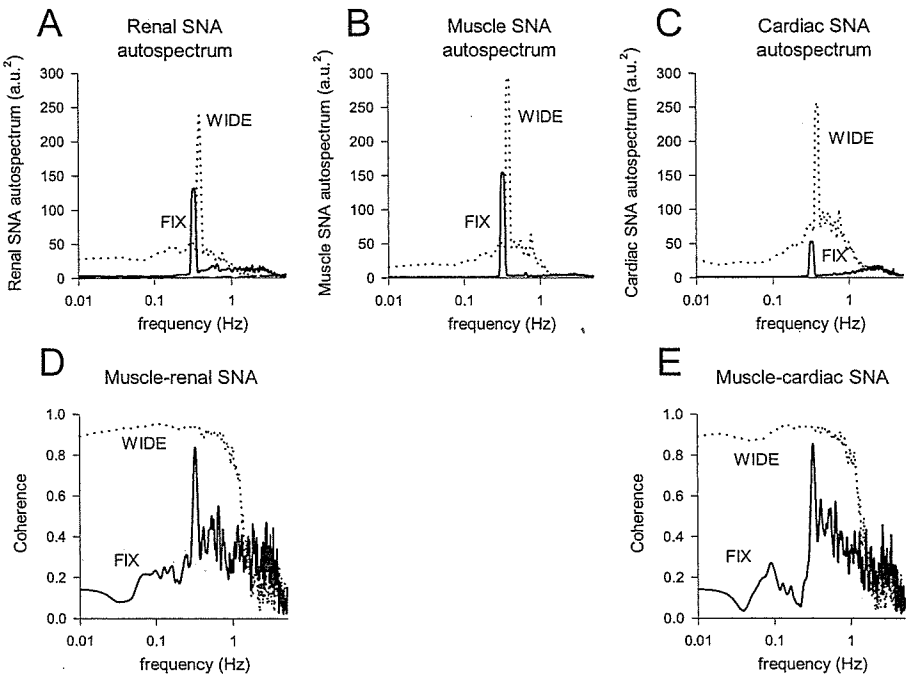

Fig. 7. Autospectra of renal (**A**), muscle (**B**), and cardiac SNAs (**C**), and the coherence function of muscle SNA against renal (**D**) and cardiac SNAs (**E**) under baroreflex open-loop conditions of WIDE (broken line) and FIX (solid line), using the same data as in Figs. 3 and 4.

muscle SNA that correlates with other SNAs, calculated as muscle SNA variance·r^2 ranked in the order of WIDE > CLOSE > FIX (Fig. 5, C and D; gray column), indicating a contribution of baroreflex-dependent regulation in maintaining homogeneity between muscle SNA and other visceral SNAs. In contrast, the variance component of muscle SNA that does not correlate with other SNAs, calculated as variance · $(1 - r^2)$, was similar among FIX, CLOSE, and WIDE (Fig. 5, C, D; black bottom column).

Frequency-domain analysis. In the same animal as in Fig. 1, the autospectra of muscle, renal, and cardiac SNAs peaked at exactly the same frequencies both in the WIDE and FIX protocols (Fig. 7, A, B, and C). Muscle SNA strongly cohered with both renal and cardiac SNAs both in WIDE and FIX at peak frequencies of the muscle SNA autospectra; however, the correlation was strong in WIDE but weak in FIX at the remaining frequencies (Fig. 7, D and E). The data of individual animals showed similar characteristics. The averaged coherence functions of all animals was consistently strong (>0.8) at peak frequencies of the muscle SNA autospectra regardless of baroreceptor pressure conditions of WIDE, CLOSE, and FIX (Fig. 8, black column). In contrast, the averaged coherence functions at the remaining frequencies were higher in WIDE (>0.8) compared with CLOSE or FIX (0.4–0.5) (Fig. 8, gray column).

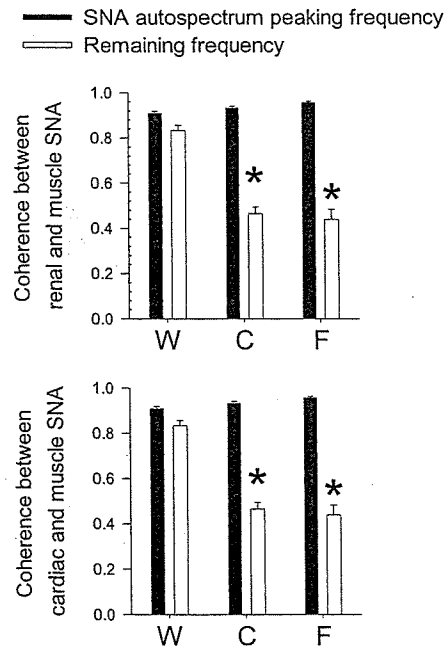

Fig. 8. Averaged coherence functions of muscle SNA against renal and cardiac SNAs at muscle SNA autospectral peak frequencies (black column) and at the remaining frequencies (gray column) under baroreceptor pressure conditions of WIDE, CLOSE, and FIX. W: WIDE; C: CLOSE; F: FIX. *P < 0.05, WIDE vs. CLOSE and FIX.

DISCUSSION

Despite the accumulating data on muscle SNA measured by microneurography in human studies, whether the neural discharge of muscle SNA correlates and coheres with that of other SNAs controlling visceral organs remains unclear. The major new findings in this study are (i) under the baroreflex closed-loop condition when CSP i matched with the systemic arterial pressure (CLOSE) muscle SNA resampled at 1 Hz correlates with both rena and cardiac SNAs in time-domain analysis (r^2: 0.6–0.7 with proper delay), and (ii) muscle SNA coheres with re nal and cardiac SNAs in frequency domain analysis, par ticularly at peak frequencies of the SNA autospectra

These results support our first hypothesis and indicate that muscle SNA correlates and coheres approximately with renal and cardiac SNAs under closed-loop baroreflex condition.

Next, although the baroreflex is known to strongly regulate muscles [3], renal and cardiac SNA [15, 20], the contribution of baroreflex to the homogeneous SNA discharges has not been elucidated quantitatively. The other major new findings in this study are as follows. When the change in baroreceptor pressure is increased from FIX (fixed CSP, no change) to CLOSE (CSP matching systemic arterial pressure, pulse pressure 30–40 mmHg) and further to WIDE (CSP fluctuating between ±40 mmHg), there are corresponding increases in the time domain correlation (r^2) of muscle SNA resampled at 1 Hz with renal and cardiac SNAs, from approximately 0.5 (FIX), to 0.6–0.7 (CLOSE), and to 0.8 (WIDE) (Fig. 5, A and B). The baroreflex dependent characteristics were also observed when SNAs were resampled at a frequency from 0.3 to 5.0 Hz (Fig. 6). This is also consistent with increases in the variance component of muscle SNA correlating with renal and cardiac SNAs (Fig. 5, C and D). These results agree with the concept that the baroreflex is important in generating harmonized SNA discharges [5, 21]. Moreover, the results indicate that arterial baroreflex has the ability to increase the homogeneity between these SNAs by nearly twofold. They support our second hypothesis and indicate that the arterial baroreflex potently homogenizes neural discharges of these SNAs.

Our results indicate that baroreflex increases the homogeneity between these SNAs by modulating SNA at nonpeak frequencies of SNA autospectra. The frequency domain correlation (coherence function) of muscle SNA with renal and cardiac SNAs was increased from approximately 0.4–0.5 (FIX), to 0.5 (CLOSE), to 0.9 (WIDE) at nonpeak frequencies, not peaking frequencies, of the SNA autospectra (Fig. 8). This suggests that other mechanisms other than baroreflex govern SNA at the nonpeak frequencies.

Our results quantitatively indicate that baroreflex-independent factors contribute to one-half of the homogeneity between muscle SNA and cardiac or renal SNA. Time-domain data show that even under a condition in which CSP is fixed at operating pressure, one-half of the variance of muscle SNAs correlates with other SNAs (Fig. 5, C and D; gray top column), with r^2 of approximately 0.5 (Fig. 5, A and B). These data indicate the presence of a baroreflex-independent component of SNA homogeneity. Although some noises may be included in the variance component of muscle SNA correlating with other SNAs, this is negligible in the calculation of variance, since the signal/noise ratio in SNA is >1,000 (noise was measured as the signal obtained after an individual animal died). The baroreflex-independent component of SNA homogeneity may be related to the strong coherence function between the SNAs at autospectral peak frequencies, since the coherence is consistently high regardless of the magnitude of baroreceptor pressure changes (Figs. 7, D and E, and 8). This component may partially be associated with the respiratory-related rhythm in sympathetic nerve discharge, a concept of central respiratory rhythm generator [21–23]. At the autospectral peak frequencies, these mechanisms may keep the coherence sufficiently high (0.9) independent of the baroreflex, and thus the baroreflex cannot increase the coherence further.

In contrast to the homogeneous sympathetic activation, the heterogeneity of muscle SNA versus renal or cardiac SNA does not relate with baroreflex. The proportions of the variance component of muscle SNA not correlating with renal and cardiac SNAs are constant regardless of the magnitude of change in baroreceptor pressure (Fig. 5, C and D). Mechanisms other than baroreflex may be involved in heterogeneous sympathetic activation. For example, chemoreflex [24], nitric oxide synthesis [25], and osmolarity [26] have been reported to produce regional differences in sympathetic activations.

Our data may strengthen the interpretation and the impact of the accumulated data on the involvement of human muscle SNA in circulatory physiology [3, 6–8, 10] and cardiovascular diseases [27, 28]. The recording of human microneurography is limited to the limbs, and there is so far little direct experimental evidence to support that muscle SNA parallel the other SNAs controlling visceral organs. The present study addresses this issue as an initial step and demonstrates the similarity between muscle SNA discharge and renal or cardiac SNA. Further study is needed to investigate the relations between SNAs in response to stimuli other than baroreflex.

Earlier studies have reported the coherence between pairs of SNA discharges for cardiac, renal, splanchnic, splenic, and lumbar SNAs in animals [29–31]. However, most of the studies focused on the coherence at frequencies faster than 1 Hz (0–15 Hz), in contrast to the present study. Furthermore, the previous studies did not measure muscle SNA or quantitatively investigate the effects of baroreflex on homogeneous SNA discharges.

Limitations

The present study has several limitations. First, anesthetic agents tend to inhibit efferent SNA and depress the gain of baroreflex control of SNA. Second, we excluded the efferent vagal nerve activities, which could affect SNA and baroreflex. Third, artificial respiration and surgical procedures used in this study may affect SNA and baroreflex. Last, based on most of the frequency domain studies of human muscle SNA [32–35], we focused on sympathetic discharge at frequencies of up to 1 Hz. And because of the low-pass characteristics of transfer function from SNA to arterial pressure (baroreflex peripheral arc) [20], the dynamic property of pressure response to

SNA becomes smaller as the frequency of SNA discharge increases. Future studies are needed to investigate the relation of muscle SNA with other SNAs at faster SNA rhythms, including a cardiac-related SNA rhythm at a frequency of 2 to 6 Hz [36] and an SNA rhythm of 10 Hz [37].

In conclusion, 1-Hz muscle SNA correlated with both renal and cardiac SNAs in time-domain analysis and cohered with renal and cardiac SNAs in frequency-domain analysis. Accompanying an increase in the magnitude of baroreceptor pressure change, both the correlation coefficient and the coherence function increased. These results indicate that muscle SNA correlates and coheres approximately with renal and cardiac SNAs under the closed-loop baroreflex condition and that the arterial baroreflex is capable of potently homogenizing neural discharges of these SNAs by modulating SNA at nonpeak frequencies of SNA autospectra.

APPENDIX

When y is scatter-plotted against x, a linear regression line can be drawn between the two variables. The Pearson product-moment correlation coefficient (r) between variables has the following relationship with variance (Eq. 1) [19]

$$r^2 = 1 - \frac{SS_{res}}{V_y} \quad (1)$$

where SS_{res} is the sum of squared deviations (residuals) from the regression line and V_y is the total sum of squared deviations from the mean of the dependent variable (y), that is, the total variance of y.

Equation 1 indicates that the square of correlation coefficient, r^2, is a fraction of the total variance in the dependent variable (y), which is explained by a linear regression relation [18, 19]. Equation 1 leads to the following relations in Eqs. 2 and 3.

$$V_y \cdot r^2 + SS_{res} = V_y \quad (2)$$

$$SS_{res} = V_y \cdot (1 - r^2) \quad (3)$$

$V_y \cdot r^2$ indicates the component of total variance in y that is explained by a linear regression relation (correlative variance in y). SS_{res} indicates the residual component of total variance in y that is not explained by linear regression relation (noncorrelative variance in y).

This study was supported by the Ground-based Research Announcement for Space Utilization project promoted by the Japan Space Forum, the research project promoted by the Ministry of Health, Labour and Welfare in Japan (#H18-nano-ippan-003), and the Grants-in-Aid for Scientific Research promoted by the Ministry of Education, Culture, Sports, Science and Technology in Japan (#18591992).

REFERENCES

1. Rowell LB. Human cardiovascular control. New York: Oxford Univ. Press; 1993.
2. Mano T. Microneurography as a tool to investigate sympathetic nerve responses to environmental stress. Aviakosmicheskaia i Ekologicheskaia Meditsina. 1997;31:8-14.
3. Wallin BG, Eckberg DL. Sympathetic transients caused by abrupt alterations of carotid baroreceptor activity in humans. Am J Physiol. 1982;242:H185-90.
4. Wallin BG, Esler M, Dorward P, Eisenhofer G, Ferrier C, Westerman R, *et al.* Simultaneous measurements of cardiac noradrenaline spillover and sympathetic outflow to skeletal muscle in humans. J Physiol (Lond). 1992;453:45-58.
5. Wallin BG, Thompson JM, Jennings GL, Esler MD. Renal noradrenaline spillover correlates with muscle sympathetic activity in humans. J Physiol (Lond). 1996;491:881-7.
6. Kamiya A, Michikami D, Fu Q, Niimi Y, Iwase S, Mano T, *et al.* Static handgrip exercise modifies arterial baroreflex control of vascular sympathetic outflow in humans. Am J Physiol Regul Integr Comp Physiol. 2001;281:R1134-9.
7. Markel TA, Daley JC, 3rd, Hogeman CS, Herr MD, Khan MH, Gray KS, *et al.* Aging and the exercise pressor reflex in humans. Circulation. 2003;107:675-8.
8. Mitchell JH, Victor RG. Neural control of the cardiovascular system: insights from muscle sympathetic nerve recordings in humans. Med Sci Sports Exerc. 1996;28(10 Suppl):S60-9.
9. Mosqueda-Garcia R, Furlan R, Tank J, Fernandez-Violante R. The elusive pathophysiology of neurally mediated syncope. Circulation. 2000;102:2898-906.
10. Tank J, Schroeder C, Diedrich A, Szczech E, Haertter S, Sharma AM, *et al.* Selective impairment in sympathetic vasomotor control with norepinephrine transporter inhibition. Circulation. 2003;107:2949-54.
11. Kamiya A, Kawada T, Yamamoto K, Michikami D, Ariumi H, Miyamoto T, *et al.* Muscle sympathetic nerve activity averaged over 1 minute parallels renal and cardiac sympathetic nerve activity in response to a forced baroreceptor pressure change. Circulation. 2005;112:384-6.
12. Kamiya A, Kawada T, Yamamoto K, Michikami D, Ariumi H, Miyamoto T, *et al.* Dynamic and static baroreflex control of muscle sympathetic nerve activity (SNA) parallels that of renal and cardiac SNA during physiological change in pressure. Am J Physiol Heart Circ Physiol. 2005;289:H2641-8.
13. Sundlof G, Wallin BG. Human muscle nerve sympathetic activity at rest. Relationship to blood pressure and age. J Physiol (Lond). 1978;274:621-37.
14. Nakamura T, Kawahara K, Kusunoki M, Feng Z. Microneurography in anesthetized rats for the measurement of sympathetic nerve activity in the sciatic nerve. J Neurosci Methods. 2003;131:35-9.
15. Kawada T, Shishido T, Inagaki M, Tatewaki T, Zheng C, Yanagiya Y, *et al.* Differential dynamic baroreflex regulation of cardiac and renal sympathetic nerve activities. Am J Physiol Heart Circ Physiol. 2001;280:H1581-90.
16. Kent BB, Drane JW, Blumenstein B, Manning JW. A mathematical model to assess changes in the baroreceptor reflex. Cardiology. 1972;57:295-310.
17. Marmarelis PZ, Marmarelis VZ. The whilte noise method in system identification. In: Analysis of Physiological Systems. New York: Plenum; 1978. p. 131-221.
18. Bendat JS, Piersol AG. Random data: analysis and measurement procedures. third edition. Canada: A Wiley-Interscience, 2000.
19. Glantz SA. Primer of biostatistics (4th ed.). New York: McGraw-Hill; 1997.
20. Ikeda Y, Kawada T, Sugimachi M, Kawaguchi O, Shishido T, Sato T, *et al.* Neural arc of baroreflex optimizes dynamic pressure regulation in achieving both stability and quickness. Am J Physiol. 1996;271:H882-90.
21. Habler HJ, Bartsch T, Janig W. Two distinct mechanisms generate the respiratory modulation in fibre activity of the rat cervical sympathetic trunk. J Auton Nerv Syst. 1996;61:116-22.
22. Morrison SF. Respiratory modulation of sympathetic nerve activity: effect of MK 801. Am J Physiol. 1996;270:R645-51.
23. Zhong S, Zhou SY, Gebber GL, Barman SM. Coupled oscillators account for the slow rhythms in sympathetic nerve discharge and phrenic nerve activity. Am J Physiol. 1997;272:R1314-24.
24. Iriki M, Dorward P, Korner PI. Baroreflex "resetting" by arterial hypoxia in the renal and cardiac sympathetic nerves of the rabbit. Pflugers Arch. 1977;370:1-7
25. Hirai T, Musch TI, Morgan DA, Kregel KC, Claassen DE, Pickar JG, *et al.* Differential sympathetic nerve responses to nitric oxide synthase inhibition in anesthetized rats. Am J Physiol. 1995;269:R807-13.
26. Weiss ML, Claassen DE, Hirai T, Kenney MJ. Nonuniform sympathetic nerve responses to intravenous hypertonic saline infusion. J Auton Nerv Syst. 1996;57:109-15.
27. Macefield VG, Rundqvist B, Sverrisdottir YB, Wallin BG, Elam M. Firing properties of single muscle vasoconstrictor neurons in the sympathoexcitation associated with congestive heart failure. Circulation. 1999;100:1708-13.

28. Narkiewicz K, van de Borne PJ, Pesek CA, Dyken ME, Montano N, Somers VK. Selective potentiation of peripheral chemoreflex sensitivity in obstructive sleep apnea. Circulation. 1999;99:1183-9.
29. Kenney MJ, Barman SM, Gebber GL, Zhong S. Differential relationships among discharges of postganglionic sympathetic nerves. Am J Physiol. 1991;260:R1159-67.
30. Kenney MJ. Frequency characteristics of sympathetic nerve discharge in anesthetized rats. Am J Physiol. 1994;267:R830-40.
31. Kenney MJ, Weiss ML, Patel KP, Wang Y, Fels RJ. Paraventricular nucleus bicuculline alters frequency components of sympathetic nerve discharge bursts. Am J Physiol Heart Circ Physiol. 2001;281:H1233-41.
32. Eckberg DL. The human respiratory gate. J Physiol. 2003;548:339-52.
33. Kamiya A, Hayano J, Kawada T, Michikami D, Yamamoto K, Ariumi H, *et al.* Low-frequency oscillation of sympathetic nerve activity decreases during development of tilt-induced syncope preceding sympathetic withdrawal and bradycardia. Am J Physiol Heart Circ Physiol. 2005;289:H1758-69.
34. Furlan R, Porta A, Costa F, Tank J, Baker L, Schiavi R, *et al.* Oscillatory patterns in sympathetic neural discharge and cardiovascular variables during orthostatic stimulus. Circulation. 2000;101:886-92.
35. Van De Borne P, Montano N, Narkiewicz K, Degaute JP, Malliani A, Pagani M, *et al.* Importance of ventilation in modulating interaction between sympathetic drive and cardiovascular variability. Am J Physiol Heart Circ Physiol. 2001;280:H722-9.
36. Barman SM, Gebber GL. "Rapid" rhythmic discharges of sympathetic nerves: sources, mechanisms of generation, and physiological relevance. J Biol Rhythms. 2000;15:365-79.
37. Barman SM, Gebber GL, Zhong S. The 10-Hz rhythm in sympathetic nerve discharge. Am J Physiol. 1992;262:R1006-14.

J. Physiol. Sci. Vol. 56, No. 3; Jun. 2006; pp. 235–245
Online Jul. 7, 2006; **doi:10.2170/physiolsci.RP006006**

Sympathetic Neural Regulation of Heart Rate Is Robust against High Plasma Catecholamines

Toru KAWADA[1], Tadayoshi MIYAMOTO[1,2], Yuichiro MIYOSHI[1], Sayo YAMAGUCHI[1], Yukiko TANABE[1], Atsunori KAMIYA[1], Toshiaki SHISHIDO[1], and Masaru SUGIMACHI[1]

[1]Department of Cardiovascular Dynamics, Advanced Medical Engineering Center, National Cardiovascular Center Research Institute, Osaka, 565-8565 Japan; and [2]Japan Association for the Advancement of Medical Equipment, Tokyo, 113-0033 Japan

Abstract: The sympathetic regulation of heart rate (HR) may be attained by neural and humoral factors. With respect to the humoral factor, plasma noradrenaline (NA) and adrenaline (Adr) can reportedly increase to levels approximately 10 times higher than resting level during severe exercise. Whether such high plasma NA or Adr interfered with the sympathetic neural regulation of HR remained unknown. We estimated the transfer function from cardiac sympathetic nerve stimulation (SNS) to HR in anesthetized and vagotomized rabbits. An intravenous administration of NA (n = 6) at 1 and 10 $\mu g \cdot kg^{-1} \cdot h^{-1}$ increased plasma NA concentration (pg/ml) from a baseline level of 438 ± 117 (mean ± SE) to 974 ± 106 and 6,830 ± 917 ($P < 0.01$), respectively. The dynamic gain (bpm/Hz) of the transfer function did not change significantly (from 7.6 ± 1.2 to 7.5 ± 1.1 and 8.1 ± 1.1), whereas mean HR (in bpm) during SNS slightly increased from 280 ± 24 to 289 ± 22 ($P < 0.01$) and 288 ± 22 ($P < 0.01$). The intravenous administration of Adr (n = 6) at 1 and 10 $\mu g \cdot kg^{-1} \cdot h^{-1}$ increased plasma Adr concentration (pg/ml) from a baseline level of 257 ± 86 to 659 ± 172 and 2,760 ± 590 ($P < 0.01$), respectively. Neither the dynamic gain (from 8.0 ± 0.6 to 8.4 ± 0.8 and 8.2 ± 1.0) nor the mean HR during SNS (from 274 ± 13 to 275 ± 13 and 274 ± 13) changed significantly. In contrast, the intravenous administration of isoproterenol (n = 6) at 10 $\mu g \cdot kg^{-1} \cdot h^{-1}$ significantly increased mean HR during SNS (from 278 ± 11 to 293 ± 9, $P < 0.01$) and blunted the transfer gain value at 0.0078 Hz (from 5.9 ± 1.0 to 1.0 ± 0.4, $P < 0.01$). In conclusion, high plasma NA or Adr hardly affected the dynamic sympathetic neural regulation of HR.

Key words: systems analysis, neuro-humoral interaction, noradrenaline, adrenaline, isoproterenol.

The sympathetic regulation of heart rate (HR) may be attained by neural and humoral factors. One unique feature of the neural regulation, which is in contrast to the humoral regulation, is its quickness. The quickness of regulation may be best quantified by identifying dynamic characteristics of the input-output or stimulus-response relationship of a given system [1, 2]. Although we have identified the dynamic characteristics of the HR regulation by the cardiac sympathetic nerve by using a transfer function analysis [3, 4], we ignored the possible effects of plasma catecholamines on the transfer function. Plasma concentrations of noradrenaline (NA) and adrenaline (Adr) can increase during systemic sympathetic activation. For instance, plasma NA and Adr both increase to approximately 10 times their respective resting levels during severe exercise [5]. They increase to approximately 6 and 20 times, respectively, during acute myocardial infarction [5]. Whether such high plasma NA or Adr interfered with the dynamic sympathetic neural regulation of HR remained unanswered.

Two mutually opposing hypotheses can be put forward regarding interactions between the humoral and neural factors in the sympathetic regulation of HR. The activation of presynaptic (or prejunctional) α_2-adrenergic receptors located on the postganglionic sympathetic nerve terminals inhibits NA release [6], which would result in the attenuated HR response to cardiac sympathetic nerve stimulation (SNS). In contrast, the activation of presynaptic (or prejunctional) β_2-adrenergic receptors located on the postganglionic sympathetic nerve terminals facilitates NA release [7], which would result in the augmented HR response to cardiac SNS. Besides these interactions, high plasma NA can increase the cardiac uptake of NA [8], which would modify the HR response to cardiac SNS.

The aim of the present study was to test the hypothesis that high plasma NA or Adr alters the dynamic sympathetic neural regulation of HR. Using anesthetized rabbits, we examined the HR response to random cardiac SNS under the condition of elevated plasma NA or Adr induced by exogenous administration. We also examined the effects of an intravenous administration of a β-adrenergic agonist isoproterenol on the HR response to SNS. The results of

Received on Jun 1, 2006; accepted on Jul 4, 2006; released online on Jul 7, 2006; doi:10.2170/physiolsci.RP006006
Correspondence should be addressed to: Toru Kawada, Department of Cardiovascular Dynamics, Advanced Medical Engineering Center, National Cardiovascular Center Research Institute, 5-7-1 Fujishirodai, Suita, Osaka, 565-8565 Japan. Phone: +81-6-6833-5012 (Ext. 2427), Fax: +81-6-6835-5403, E-mail: torukawa@res.ncvc.go.jp

the present study indicated that high plasma NA or Adr hardly affected the dynamic sympathetic neural regulation of HR in anesthetized rabbits.

MATERIALS AND METHODS

Animal preparation. The animals were cared for in strict accordance with the Guiding Principles for the Care and Use of Animals in the Field of Physiological Sciences approved by the Physiological Society of Japan. Eighteen Japanese white rabbits weighing from 2.4 to 3.2 kg were anesthetized by a mixture of α-chloralose (40 mg/ml) and urethane (250 mg/ml), initiated with a bolus injection of 2 ml/kg and maintained with a continuous administration at 0.5 $ml \cdot kg^{-1} \cdot h^{-1}$. The rabbits were intubated and mechanically ventilated with oxygen-enriched room air. The right cardiac postganglionic sympathetic nerve was identified in the right thoracic cavity and sectioned. Usually, HR dropped immediately after the sectioning of the right cardiac sympathetic nerve, suggesting the importance of the right cardiac sympathetic nerve in determining baseline HR. A pair of platinum electrodes was attached to the cardiac end of the sectioned nerve for stimulation. The nerve and electrodes were secured by silicone glue (Kwik-Sil, World Precision Instruments, Sarasota, FL, USA). The left cardiac sympathetic nerve and other sympathetic branches to the heart were kept intact. The carotid sinus nerves and aortic depressor nerves were sectioned bilaterally to minimize changes in systemic sympathetic activity induced by baroreflexes. The vagal nerves were also sectioned bilaterally to eliminate the vagal effect on the heart. The vagotomy did not change HR significantly at this stage, possibly because of the vagolitic effects of the anesthesia. Arterial pressure (AP) was measured by a micromanometer (Millar Instruments, Houston, TX, USA) inserted into the thoracic aorta from the right femoral artery. HR was measured with a cardiotachometer (AT-601G, Nihon Kohden, Tokyo, Japan). An arterial catheter was inserted into the left femoral artery to sample blood for plasma catecholamine measurements. A double-lumen venous catheter was introduced into the right femoral vein for continuous anesthetic infusion and exogenous catecholamine administration.

Protocols. We quantified the dynamic sympathetic neural regulation of HR by using a transfer function analysis [3, 4]. To estimate the transfer function from cardiac SNS to HR, we dynamically stimulated the right cardiac sympathetic nerve as follows. The pulse duration was set at 2 ms, and the pulse amplitude was adjusted to obtain an HR increase of approximately 50 bpm (beats/min) during a 5-Hz constant stimulation in each animal. The resulting amplitude ranged from 0.8 to 2.0 V among animals. With these settings, the stimulation frequency was randomly assigned at either 0 or 5 Hz every 2 s, according to a binary white noise sequence (see appendix A for additional information). The average stimulation frequency was therefore 2.5 Hz. The input power spectral density of SNS was relatively flat up to 0.25 Hz.

In *Protocol 1* ($n = 6$), physiological saline was infused intravenously at 1 $ml \cdot kg^{-1} \cdot h^{-1}$ for 30 min after the end of surgical preparation (Fig. 1). A 300-μl volume of arterial blood was sampled under control conditions (designated as NA_0 condition) for plasma catecholamine measurements. Following the blood sampling, dynamic SNS was applied for 15 min to estimate the transfer function from SNS to HR. Arterial blood was sampled during the last minute of dynamic SNS under the NA_0 condition. Next, 1-μg/ml NA solution was infused at 1 $\mu g \cdot kg^{-1} \cdot h^{-1}$ (NA_1). Fifteen min after the initiation of NA_1 administration, when AP and HR had reached new steady states, arterial blood sampling and 15-min dynamic SNS were repeated. Third, a 10-μg/ml NA solution was administered at 10 $\mu g \cdot kg^{-1} \cdot h^{-1}$ (NA_{10}). Fifteen min after the initiation of NA_{10} administration, arterial blood sampling and 15-min dynamic SNS were repeated.

In *Protocol 2* ($n = 6$), experimental procedures similar to those in *Protocol 1* were conducted, using the Adr solution instead of the NA solution. The transfer function from SNS to HR was estimated under control condition (designated as Adr_0 condition), as well as during the administration of 1-μg/ml Adr solution at 1 $\mu g \cdot kg^{-1} \cdot h^{-1}$ (Adr_1) and 10-μg/ml Adr solution at 10 $\mu g \cdot kg^{-1} \cdot h^{-1}$ (Adr_{10}).

In *Protocol 3* ($n = 6$), we examined the effects of an intravenous administration of a β-adrenergic agonist isoproterenol on the transfer function from SNS to HR. Using experimental procedures similar to those in *Protocol 1*, we

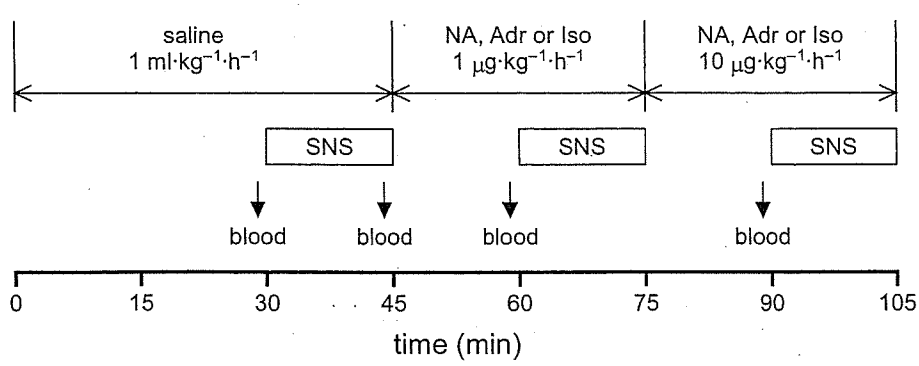

Fig. 1. Schematic diagram showing the experimental protocol. The downward arrows indicate the timings of blood sampling for catecholamine measurements (for *Protocols 1* and *2*). SNS: sympathetic nerve stimulation. NA: noradrenaline; Adr: adrenaline; Iso: isoproterenol.

administered 1-μg/ml isoproterenol solution at 1 μg·kg^{-1}·h^{-1} (Iso_1) and 10-μg/ml isoproterenol solution at 10 μg·kg^{-1}·h^{-1} (Iso_{10}) and estimated the transfer function under the control (designated as Iso_0), Iso_1, and Iso_{10} conditions.

Data analysis. The SNS command and HR were stored at a sampling rate of 200 Hz. The data were analyzed from only 2 min after the initiation of SNS to remove the initial trend of the HR increase. To estimate the transfer function from SNS to HR, we resampled the SNS-HR data pairs at 8 Hz. These data were segmented into 10 sets of half-overlapping bins of 1,024 data points each. In each segment, a linear trend was subtracted and a Hanning window was applied. The fast Fourier transform was then applied to obtain the frequency spectra of SNS and HR [9]. We calculated the ensemble averages of input power spectral density [$S_{SNS\cdot SNS}(f)$], output power spectral density [$S_{HR\cdot HR}(f)$], and cross-spectral density between the input and output [$S_{HR\cdot SNS}(f)$]. The transfer function [$H(f)$] was estimated using the following equation [10, 11].

$$H(f) = \frac{S_{HR\cdot SNS}(f)}{S_{SNS\cdot SNS}(f)} \tag{1}$$

We also calculated the magnitude-squared coherence function [$Coh(f)$] using the following equation [10, 11].

$$Coh(f) = \frac{\left|S_{HR\cdot SNS}(f)\right|^2}{S_{SNS\cdot SNS}(f)\, S_{HR\cdot HR}(f)} \tag{2}$$

The coherence function is a frequency-domain measure of the linear dependence between the input and output signals. A unity coherence value indicates a perfect linear dependence of HR on SNS, whereas a zero coherence value indicates the total independence between SNS and HR.

In *Protocols 1* and *2*, the transfer function from SNS to HR was parameterized by using a mathematical model [$H_m(f)$] of a second-order low-pass filter with pure dead time, using the following equation [3, 12].

$$H_m(f) = \frac{K}{1 + 2\zeta \frac{f}{f_N} j + \left(\frac{f}{f_N} j\right)^2} \exp(-2\pi f\, jL) \tag{3}$$

where K is the dynamic gain (in bpm/Hz), f_N is the natural frequency (in Hz), ζ is the damping ratio, and L is the pure dead time (in s); j represents the imaginary unit (see appendix B for details). A nonlinear iterative least square fitting was performed to minimize the following error function.

$$err = \frac{\sum_{i=1}^{N} \left|H(f_i) - H_m(f_i)\right|^2}{\sum_{i=1}^{N} \left|H(f_i)\right|^2}, \quad f_i = f_0 \times i \tag{4}$$

where f_0 indicates the fundamental frequency of the Fourier transform. N specifies the upper frequency bound of the fitting procedure. We set N at 32 so as to fit $H_m(f)$ to $H(f)$ up to 0.25 Hz.

In *Protocol 3*, because the transfer function from SNS to HR during Iso_{10} was significantly deviated from the mathematical model of a second-order low-pass filter with pure dead time (Eq. 3), we did not fit the mathematical model to the transfer function and adopted the transfer gain values at the lowest frequency ($G_{0.0078}$) and at 0.1 Hz ($G_{0.1}$) to represent the frequency response of HR to SNS.

Catecholamine measurements. The arterial blood sample was centrifuged and a 100-μl volume of plasma was obtained. The plasma was transferred into a 1.5-ml polypropylene conical tube. A 50-μl volume of the working internal standard solution [100 pg of 3,4-dihydroxybenzylamine (DHBA)], 5 mg of acid-washed alumina, and 1.0 ml of 1-M tris(hydroxymethyl) aminomethane buffer (pH 8.6), containing 0.2% disodium ethylendiaminetetraacetic acid (EDTA), was added to the conical tube and shaken for 15 min. After shaking, the alumina was washed three times with distilled water, transferred into a microfilter (Ultrafree C3, Millipore, Bedford, MA), and centrifuged to remove excess fluid. NA, Adr, and DHBA were then eluted from the alumina, using 60 μl of 2% acetic acid, and their concentrations were measured by using high-performance liquid chromatography with electrochemical detection (DTA-300, Eicom, Kyoto, Japan). Plasma NA and Adr concentrations were calculated, taking into account the recovery rate of DHBA.

Statistical analysis. All data are presented in mean and mean ± SEM values. In *Protocol 1*, the effect of dynamic SNS on the plasma NA concentration was examined by a paired t-test under NA_0 condition. The NA and Adr concentrations before SNS were compared among NA_0, NA_1, and NA_{10} conditions, using Dunnett's test against a single control following the repeated-measures analysis of variance [13]. We also compared mean HR, mean AP, and parameters of the transfer function among NA_0, NA_1, and NA_{10} conditions, using Dunnett's test following repeated-measures analysis of variance. In *Protocol 2*, the effect of dynamic SNS on the plasma Adr concentration was examined by a paired t-test under Adr_0 condition. Other values, including plasma NA and Adr concentrations, mean HR, mean AP, and parameters of the transfer function, were compared among Adr_0, Adr_1, and Adr_{10} conditions, using Dunnett's test following repeated-measures analysis of variance. In *Protocol 3*, mean HR, mean AP, and gain values ($G_{0.0078}$ and $G_{0.1}$) were compared among Iso_0, Iso_1,

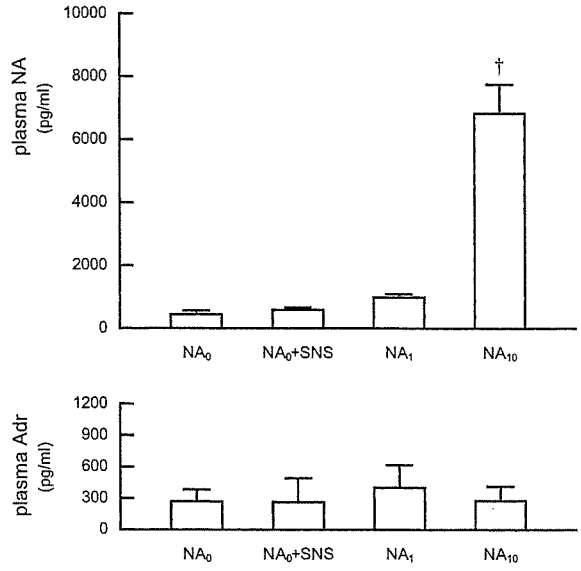

Fig. 2. Plasma concentrations of NA and Adr obtained from *Protocol 1*. The plasma NA concentration was significantly increased during the NA_{10} condition. The plasma Adr concentration was not changed significantly by the NA infusion. NA_0: saline infusion; NA_1 and NA_{10}: noradrenaline infusions at 1 and 10 μg·kg^{-1}·h^{-1}.

and Iso_{10} conditions, using Dunnett's test following repeated-measures analysis of variance. In all of the statistics, the difference was considered significant at $P < 0.05$.

RESULTS

Effects of high plasma NA on the dynamic sympathetic neural regulation of HR

In *Protocol 1*, dynamic SNS for 15 min did not change the plasma NA or Adr concentration significantly during NA_0 condition (Fig. 2, NA_0 vs. NA_0+SNS). The plasma NA concentration prior to dynamic SNS did not increase significantly during NA_1 condition, but increased to approximately 15 times higher during NA_{10} condition compared to NA_0 condition. The NA infusion did not significantly affect the plasma Adr concentration.

Figure 3A illustrates the time series of SNS, HR, and AP under NA_0, NA_1, and NA_{10} conditions obtained from one animal. The SNS was assigned at 0 or 5 Hz according to a binary white noise sequence. HR changed randomly in response to the dynamic SNS. Mean HR was slightly increased during NA infusion, whereas the amplitude of HR variation appeared unchanged. Mean AP was increased during NA_{10} condition compared to NA_0 condition.

Figure 3B shows averaged transfer functions from SNS to HR during NA_0, NA_1, and NA_{10} conditions obtained from all six animals in *Protocol 1*. The solid curve and the dashed curves in each plot represent mean and mean ± SEM values, respectively. In the gain plot, the transfer

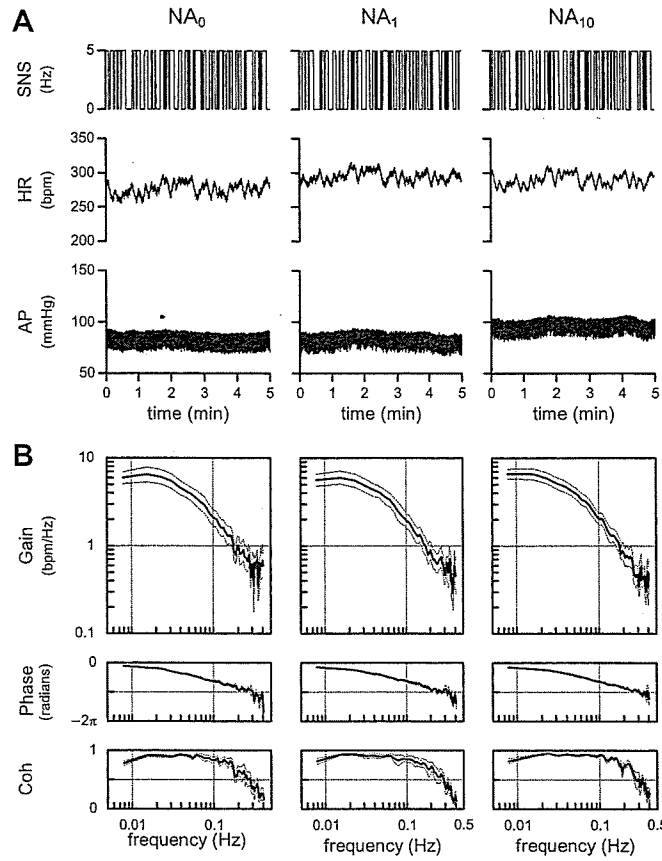

Fig. 3. A: Time series of one animal obtained from *Protocol 1*. Sympathetic nerve stimulation (SNS), heart rate (HR), and arterial pressure (AP) are shown. HR changed dynamically in response to SNS. **B**: Averaged transfer functions from SNS to HR during NA_0, NA_1, and NA_{10} conditions obtained from *Protocol 1* (n = 6). NA infusion did not affect the transfer function significantly except for changes in the damping ratio. Solid and dashed curves indicate mean and mean ± SEM values, respectively.

gain decreased with increasing frequency, reflecting the low-pass characteristics of the sympathetic neural regulation of HR. In the phase plot, the phase was near zero radians at the lowest frequency and delayed with increasing frequency, reflecting the SNS increases of HR. In the coherence plot, high coherence values up to 0.2 Hz indicate that approximately 80% of the HR variation in this frequency range was explained by the linear dynamics between SNS and HR. The transfer functions were similar among the three conditions. The dynamic gain, natural frequency, and pure dead time did not differ among the three conditions (Table 1). However, the damping ratio was significantly greater during NA_1 and NA_{10} conditions compared to the NA_0 condition.

Mean HR before SNS did not differ among NA_0, NA_1, and NA_{10} conditions, whereas mean HR during SNS increased significantly during NA_1 and NA_{10} conditions compared to NA_0 condition (Table 1). Although the repeated-measures analysis of variance indicated that the ef-